AGU PUBLICATIONS

Geochemistry, Geophysics, Geosystems

RESEARCH ARTICLE
10.1002/2015GC005766

Water input and water release from the subducting Nazca Plate along southern Central Chile (33°S–46°S)

David Völker[1,2] and Michael Stipp[2]

[1]MARUM Center for Marine Environmental Sciences, University of Bremen, Bremen, Germany, [2]Collaborative Research Center (SFB) 574 at the GEOMAR Helmholtz Centre for Ocean Research Kiel, Kiel, Germany

Key Points:
- Water budget of the subduction zone of southern Central Chile is calculated
- High flux variability is observed over short distance of <1500 km
- Subduction zones cannot be treated as entities when calculating global budgets

Supporting Information:
- Supporting Information S1
- Supporting Information S2a
- Supporting Information S2b
- Supporting Information S2c

Correspondence to:
D. Völker,
dvoelker@marum.de

Citation:
Völker, D., and M. Stipp (2015), Water input and water release from the subducting Nazca Plate along southern Central Chile (33°S–46°S), *Geochem. Geophys. Geosyst.*, *16*, 1825–1847, doi:10.1002/2015GC005766.

Received 6 FEB 2015
Accepted 6 MAY 2015
Accepted article online 12 MAY 2015
Published online 16 JUN 2015

Abstract The age of the subducting Nazca Plate off Chile increases northward from 0 Ma at the Chile Triple Junction (46°S) to 37 Ma at the latitude of Valparaíso (32°S). Age-related variations in the thermal state of the subducting plate impact on (a) the water influx to the subduction zone, as well as on (b) the volumes of water that are released under the continental fore arc or, alternatively, carried beyond the arc. Southern Central Chile is an ideal setting to study this effect, because other factors for the subduction zone water budget appear constant. We determine the water influx by calculating the crustal water uptake and by modeling the upper mantle serpentinization at the outer rise of the Chile Trench. The water release under fore arc and arc is determined by coupling FEM thermal models of the subducting plate with stability fields of water-releasing mineral reactions for upper and lower crust and hydrated mantle. Results show that both the influx of water stored in, and the outflux of water released from upper crust, lower crust, and mantle vary drastically over segment boundaries. In particular, the oldest and coldest segments carry roughly twice as much water into the subduction zone as the youngest and hottest segments, but their release flux to the fore arc is only about one fourth of the latter. This high variability over a subduction zone of <1500 km length shows that it is insufficient to consider subduction zones as uniform entities in global estimates of subduction zone fluxes.

1. Introduction

Water is carried into subduction zones with the subducting oceanic plate (1) as sedimentary pore water, (2) bound to mineral phases of the subducting sediments, (3) in pores of the oceanic crust and mantle, (4) bound to mineral phases of the crust, and (5) bound to minerals of the upper lithospheric mantle [e.g., *van Keken et al.*, 2011]. It is assumed that most of the water that comes in with sediments and particularly the sedimentary pore water is released in early phases of the subduction process and over the first kilometers of subduction [e.g., *Gieskes et al.*, 1990; *Brown et al.*, 2001; *Saffer*, 2003]. In contrast, the other constituents of the subduction zone water input have the potential to dive deep into the subduction zone and to become released under the fore arc, arc or to get recycled into the continental mantle. They are the subject of this paper.

After the creation of oceanic crust, its hydration and the development of its pore space are processes that depend on crustal age [*Jarrard*, 2003]. The hydration of the lithospheric mantle is mainly related to the formation of serpentine when upper mantle rocks are in contact with seawater at temperatures below ~500°C. Serpentine acts as the major reservoir and carrier of water within the upper mantle. Serpentinization of the oceanic mantle depends on the availability of water by deep circulation and on the mantle temperature, and thus the lithospheric age [*Iyer et al.*, 2012]. A considerable part of this serpentinization occurs at the outer rise (or forebulge) of subduction zones where normal faulting related to plate bending creates pathways for the descent of fluids [e.g., *Ranero et al.*, 2003; *Peacock et al.*, 2005; *Grevemeyer et al.*, 2007]. The degree and extent of serpentinization that develops during bending-related faulting at the trench outer rise has been studied in Central America and Chile based on seismic mantle velocities [*Ivandic et al.*, 2008, 2010; *Lefeld et al.*, 2009; *Contreras-Reyes et al.*, 2007, 2008].

The water release from crust and mantle in subduction zones depends fundamentally on the temperatures that are met along the subduction path, as the important dehydration reactions are predominantly

thermally controlled. Those temperature conditions and, to a lesser degree, pressure conditions therefore define the depth and the position relative to the arc where water is set free from the subducting slab.

The southern Central Chile subduction zone forms an ideal setting for studying the water release from a subducting slab, as the age of the subducting Nazca Plate and therefore its thermal character changes significantly from the Chile Triple Junction at 46°S (age of close to zero, very high geothermal gradient) to its northern end at 31°S (age of 37 Ma, low geothermal gradient), whereas other plate tectonic constraints (rate and angle of subduction, bathymetric roughness, and crustal thickness of the subducting Nazca Plate, thickness of Nazca Plate sediment cover) do not vary significantly [e.g., *Völker et al*., 2011a; *Contreras-Reyes et al*., 2007, 2008; *Scherwath et al*., 2009; *Syracuse et al*., 2010].

In this paper, we calculate the amount of water that is carried into the south-central Chilean subduction zone (33°S–46°S) by the oceanic crust and mantle for five Nazca Plate segments of different age. Together, the segments have a length of 1480 km, corresponding to ∼3.33% of the total length of active subduction zones of the world (44,450 km, according to *Jarrard* [2003]). We run thermal models for those segments and map the calculated P-T conditions onto stability fields of mineral reactions in the upper and lower crust and mantle that are important for the release of water. Together with an estimation of the initial water content over the depth of the subducting slab, we calculate (1) where portions of the subducted water are being released by mineralogical reactions and (2) how much of water is set free or, alternatively, retained in the slab and carried beyond the volcanic arc.

2. Geotectonic Setting

The convergent continental margin of southern Central Chile (33°S–46°S) is characterized by the subduction of the oceanic Nazca Plate under the continental South American Plate (Figure 1). Plate convergence is slightly oblique with a rate of 6.6 cm/yr at a direction of 80.1° [*Angermann et al*., 1999], respectively, 6.65 cm/yr at 82.4° [*Kendrick et al*., 2003]. The age of the Nazca Plate at the deformation front increases from the Chile Triple Junction at 46°S, where crust is being created and immediately subducted to about 37 My at the northern end of the working area at 33°S [*Tebbens et al*., 1997]. Thus, the slab thermal parameter Φ [*Kirby et al*., 1991], defined as the product of slab age and convergence speed ranges from 0 at the Chile Triple Junction to 2600 km at the latitude of Valparaiso, which is low to intermediate on global scale. Sediments covering the incoming Nazca Plate and the fill of the Chile Trench are accreted to a small accretionary prism of the Chilean fore arc. North of 38°S, tectonic erosion of the continental fore arc is taking place concomitant to the buildup of a small accretionary prism according to *Stern* [2011].

Three large fracture zones (Valdivia FZ, Chiloé FZ, and Guafo FZ) are aligned roughly perpendicular to the trench, while Mocha FZ has a more oblique trend (Figure 1). As these fracture zones delimit major age discontinuities of the Nazca Plate, they define five Nazca Plate segments of different age (Table 1). North of the Valdivia FZ, the oceanic plate was formed at the Pacific-Farallon Spreading Center more than 20 Ma ago [*Müller et al*., 2008], whereas south of the Valdivia FZ it was created at the Chile Rise within the past 20 Ma [*Herron et al*., 1981]. Both, the Chile Rise and the Pacific-Farallon Spreading Center are intermediate to fast-spreading ridges. The crustal thickness in the study area ranges between ∼4 and 7 km in general [*Scherwath et al*., 2009; *Contreras-Reyes et al*., 2007]. At ∼45°S, close to the Chile Rise, the oceanic crust consists of a 3–3.5 km thick mafic basement and a 1 km thick sediment trench fill layer on top. In the central part of the study area, between 42°S and 37°S the basement thickness increases from ∼4 to about 5.5 km and the sediments from ∼1.5 to 1.8 km (TIPTEQ data) [*Scherwath et al*., 2009]. In the northern part of the study area at around 33°S, the crust comprises a basement of ∼5 km (CONDOR data) [*Flueh et al*., 1998] and a sediment layer of ∼1.5 km in the trench [*Völker et al*., 2013].

On land, the present volcanic arc is delineated by the Southern Volcanic Zone (SVZ) within the Andean Cordillera with at least 60 historically active volcanic edifices in Chile and Argentina and numerous minor eruptive centers [*Siebert and Simkin*, 2002; *Stern*, 2004, 2007]. The northern end of the SVZ coincides with the on-land projection of the subducting Juan Fernandez Ridge, a seamount chain on the Nazca Plate (Figure 1). The southern end is defined by the subducting Chile Rise (Figure 1). The volcanism indicates that there is probably a significant release of fluids from the down-going plate and that these fluids likely enter the mantle wedge of the overriding plate, causing partial melting [e.g., *Sisson and Grove*, 1993; *Grove et al*., 2006]. The dehydration reactions that release most of the free water are described in the following section.

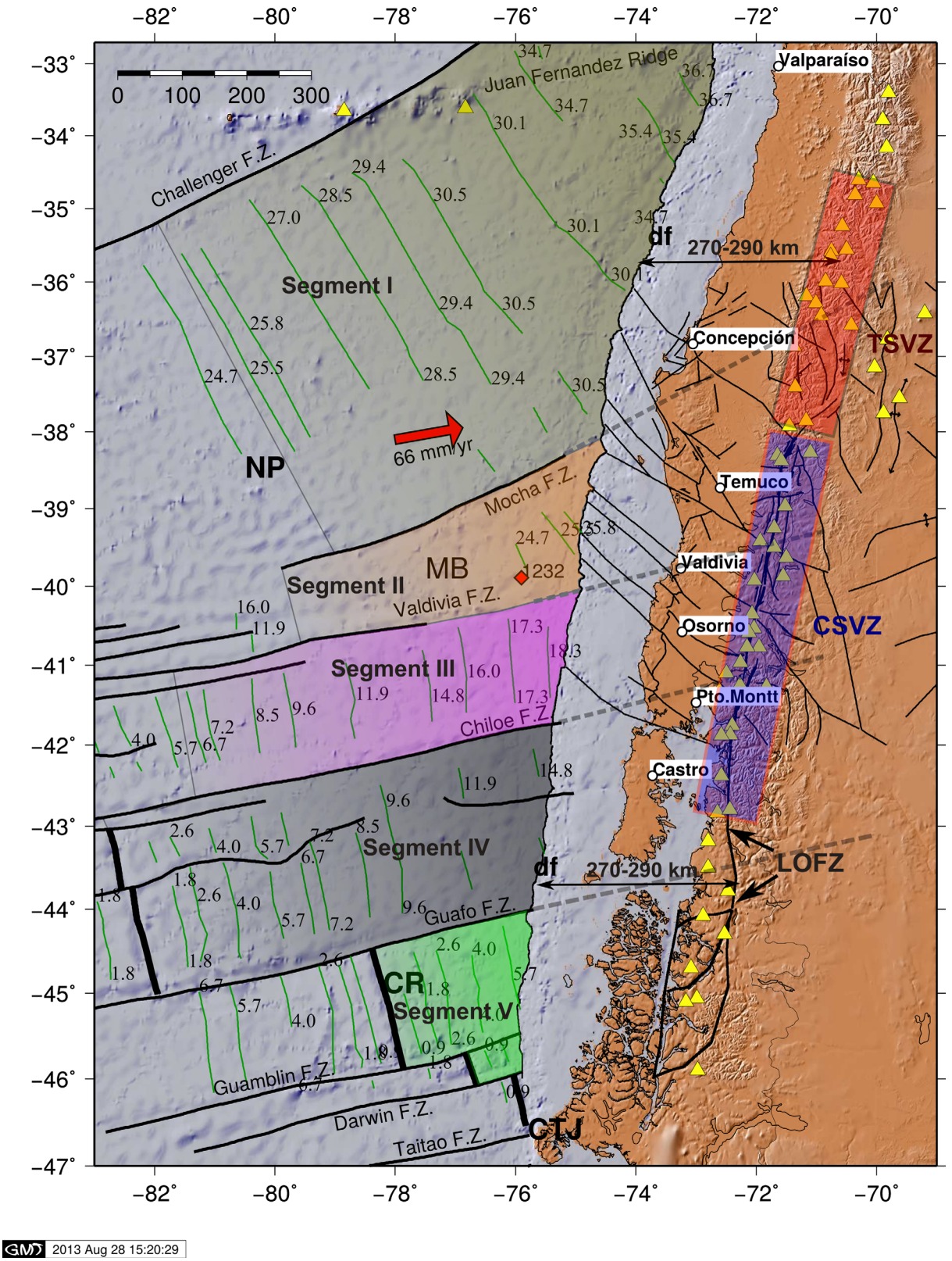

Figure 1. Overview map of Southern Central Chile and the Southern Volcanic Zone of Chile. The Nazca Plate isochrones (green lines, age in Ma) are adapted from *Tebbens et al.* [1997]. The Nazca Plate age segments as given in Table 2 are color-indicated. On land, prominent upper plate faults between 36°S and 42°S as published by *Melnick and Echtler* [2006] are drawn as black lines. NP = Nazca Plate, CR = Chile Rise, CTJ = Chile Triple Junction, MB = Mocha Block, LOFZ = Liquini-Ofqui Fault Zone, LFZ = Lanalhue Fault Zone, CSVZ = Central Southern Volcanic Zone, TSVZ = Transitional Southern Volcanic Zone. The Nazca Plate segments for which water budgets are calculated are color-coded in agreement with later figures.

Table 1. Nazca Plate Segments That are Subducting Underneath Southern Central Chile

Name	Position	Latitude	Length	Crustal Age at the Outer Rise
Segments of the Subducting Nazca Plate off Southern Central Chile				
Segment 1	N of Mocha FZ	33°S–38°S	550 km	30 Ma
Segment 2	Between Mocha FZ and Valdivia FZ	38°S–40°S	225 km	25 Ma
Segment 3	Between Valdivia and Chiloé FZ,	40°S–41.5°S	170 km	17.3 Ma
Segment 4	Between Chiloé FZ and Guafo FZ	41.5°S–43.5°S	225 km	12.5 Ma
Segment 5	South of Guafo FZ	43.5°S–46°S	280 km	4 Ma

3. Breakdown of Hydrous Mineral Phases Along the Subduction Path

3.1. Oceanic Crust

Basalt is the predominant lithology of the oceanic crust in the form of lava flows, pillow lavas, sills, dikes, tuff layers, and hyaloclastites. Other mafic rock types (e.g., gabbros from the "ophiolite sequence") are similar in mineral composition and hence are mineralogically represented by basalt in this study. The sediment cover on top of the incoming Nazca Plate is thin (<200 m seaward of the trench). The stack of trench sediment that gets thrust under, and incorporated into the frontal prism varies in thickness between 1500 and 1000 m, but only a fraction of that stack appears to dive deep into the subduction zone [*Contreras-Reyes et al*., 2010; *Geersen et al*., 2011]. The sediment pore water is released early and dehydration of the sedimentary minerals occurs largely during low-grade metamorphism in or below the fore-arc wedge. Therefore, and because of the small amount of sediments being subducted not much water resides within the sediments to depths >10 km. Accordingly, most of the volatiles of the oceanic crust are released from the metabasalts [e.g., *Staudigel et al*., 1996; *Kerrick and Connolly*, 2001], predominantly by dehydration reactions. The first water gain of the metabasalts takes place during ocean floor metamorphism directly following magmatic emplacement and cooling to subsolidus conditions [e.g., *Tomasson and Kristmansdottir*, 1972; *Humphris and Thompson*, 1978; *Natland and Dick*, 2001]. Offshore south-central Chile, further uptake of water appears to occur during bend faulting [*Contreras-Reyes et al*., 2007]. The water content of the metabasalts depends on water availability and the grade and duration of metamorphic alteration, making an absolute quantification difficult or impossible, as will be described below in the hydration model of the mafic crust.

The lowest temperature metamorphic mineral assemblage (subgreenschist facies) is the first to be decomposed. Dehydration reactions are preferentially temperature-dependent, but also pressure-dependent for metamafic rocks (see preferred trend of reaction isograds in supporting information Figure S2). The lowest temperature metamorphic mineral assemblage (subgreenschist facies) is the first to be decomposed. Most water is released by the decomposition of the zeolite minerals and analcite [e.g., *Coombs et al*., 1959; *Thompson*, 1971; *Frey et al*., 1991]. See supporting information Figures S2a and S2b, for the described mineral stability and reactions. At temperatures >~300°C, prehnite, and at higher confining pressure pumpellyite are converted to assemblages containing zoisite, lawsonite, grossular, tremolite, and/or chlorite with

Table 2. Initial Composition of Metabasalts and Serpentinized Mantle in Oxide Notation[a]

Component by wt %	Metabasalt [*Staudigel et al*., 1996]	Upper Crust (600 m), Adapted From *Staudigel et al.* [1996]	Lower Crust (600–5000 m), Adapted From *Staudigel et al.* [1996]	Serpentinized Mantle [*Kerrick and Connolly*, 1998]
Initial Composition of Crust and Mantle				
SiO_2	45.8	43.41	46.31	44.5
TiO_2	1.18	1.12	1.19	
Al_2O_3	15.53	14.72	15.70	1.7
FeO	9.69	9.18	9.80	9.6
MgO	6.66	6.31	6.73	42.6
CaO	12.88	12.21	13.02	1.4
Na_2O	2.07	1.96	2.09	
K_2O	0.56	0.53	0.57	
H_2O	**2.68**	**7.76**	**1.60**	**5.8**
CO_2	2.95	2.80	2.98	
Sum	100	100	100	

[a]The initial water content is highlighted in boldface.

excess water and quartz. This is characteristic for the subgreenschist to greenschist facies transition in hot subduction settings, present in the southern part of the study area [e.g., *Springer et al*., 1992; *Powell et al*., 1993; *Digel and Gordon*, 1995]. When the geothermal gradient is low, as in cold subduction zones, and maybe in the northern part of the study area, subgreenschist facies are directly transformed into blueschist facies mineral assemblages [e.g., *Ernst*, 1972; *Janots et al*., 2006]. This transition is mostly pressure controlled and occurs for maximal 300°C at confining pressures between 0.6 and 0.8 GPa.

Within greenschist facies conditions water is released by the reduction of the phyllosilicates chlorite, margarite, pyrophyllite, celadonite, muscovite as well as epidote/zoisite, and/or actinolite/tremolite [e.g., *Will et al*., 1990; *Ukar and Cloos*, 2014]. Depending on initial composition, retrogression, and subduction path of the rocks, only a few of these minerals might be present. At higher pressures, kyanite, tremolite, zoisite, and the phyllosilicates phengite, paragonite, and phlogopite remain predominant and water is mainly released by the decomposition of the lower pressure phyllosilicates.

Blueschist facies metamorphic conditions are either achieved directly from the subgreenschist facies during cold subduction as described before or from the greenschist facies during hot subduction at temperatures between 300 and 500°C and confining pressures between 0.8 and 1.1 GPa [e.g., *Ernst*, 1972; *Matthews and Schliestedt*, 1984]. When glaucophane, zoisite, or paragonite are produced out of the paragenesis tremolite, albite, and chlorite additional water is released. Toward higher blueschist facies conditions, the breakdown of lawsonite with its crystal water represents a significant water discharge, especially important for hot subduction. The decomposition of chlorite, paragonite, and other higher pressure phyllosilicates delivers additional amounts of water [*Peacock*, 1993; *Poli and Schmidt*, 1995; *Liu et al*., 1996; *Ono*, 1998; *Tsujimori and Ernst*, 2014].

The blueschist to eclogite-transition is characterized by glaucophane + paragonite turning into jadeite/omphacite + garnet (pyrope-rich) + quartz and water [e.g., *Patrick and Day*, 1989]. The negative slope of this reaction on a p/T-diagram causes a lower pressure transition to the eclogite facies for hot subduction at approximately 1.4 GPa and 550°C and a higher pressure transition for cold subduction between 1.7 and 2.0 GPa and 400–500°C. Further water is expelled by the breakdown of chloritoid, chlorite, phengite, zoisite, and talc within eclogite facies conditions [e.g., *Bearth*, 1963; *Hirajima et al*., 1988]. In low temperature eclogites also lawsonite and even glaucophane persist up to confining pressures of 3.0–3.5 GPa [e.g., *Kerrick and Connolly*, 2001]. All these hydrous phases become unstable at more temperature-accentuated conditions. The last stoichiometric water might be bound to K-bearing Na-Ca-amphiboles, which form due to the decomposition of phengite at higher temperature eclogite facies conditions [*Triboulet*, 1992].

3.2. Mantle Rocks

We assume that a variably hydrated, depleted peridotite containing chrysotile and brucite or talc is a probable starting material for subducting mantle rock [e.g., *Evans*, 1977; *Bucher and Frey*, 2002]. The degree of initial serpentinization depends on the water availability and the PT conditions the peridotite was previously exposed to [cf. *Martin and Fyfe*, 1970; *Okamoto et al*., 2011; *Iyer et al*., 2012] as is outlined in our model of upper mantle serpentinization. With prograde metamorphism in the subduction zone, the hydrated mineral phases are decomposed, releasing water during each reaction. In contrast to retrograde reaction paths when a metastable peridotite assemblage of olivine, ortho and clinopyroxene is preserved, the prograde reactions effectively dehydrate the entire rock on the way to the peridotite stability field. For the ultramafic rocks, the dehydration reactions are mainly temperature-dependent, whereas the dehydration of metabasalts shows a significant pressure-dependence.

For the oceanic mantle rocks dehydration reactions above 400–450°C are relevant, conditions at which first forsterite is formed and stable with decomposing antigorite [e.g., *Trommsdorff and Evans*, 1972; *Evans et al*., 1976; *Wunder and Schreyer*, 1997; *Padron-Navarta et al*., 2010]. See supporting information Figure S2c, for the described mineral stability and reactions. Brucite is unstable under these temperature conditions. The last antigorite determines the upper thermal stability limit for serpentinites at approximately 600°C at the given elevated pressure conditions [*Evans et al*., 1976; *Ulmer and Trommsdorff*, 1995; *Wunder and Schreyer*, 1997]. Deserpentinization is complete at this point and most of the water is released, in particular if the initial material is serpentinite [*Hacker et al*., 2003a]. The breakdown of talc at subduction zone pressure conditions is another source of water at 650–700°C [*Pawley et al*., 1995]. If amphibole (tremolite and clinoamphibole) and chlorite—characteristic for a less depleted, more lherzolithic initial composition—are

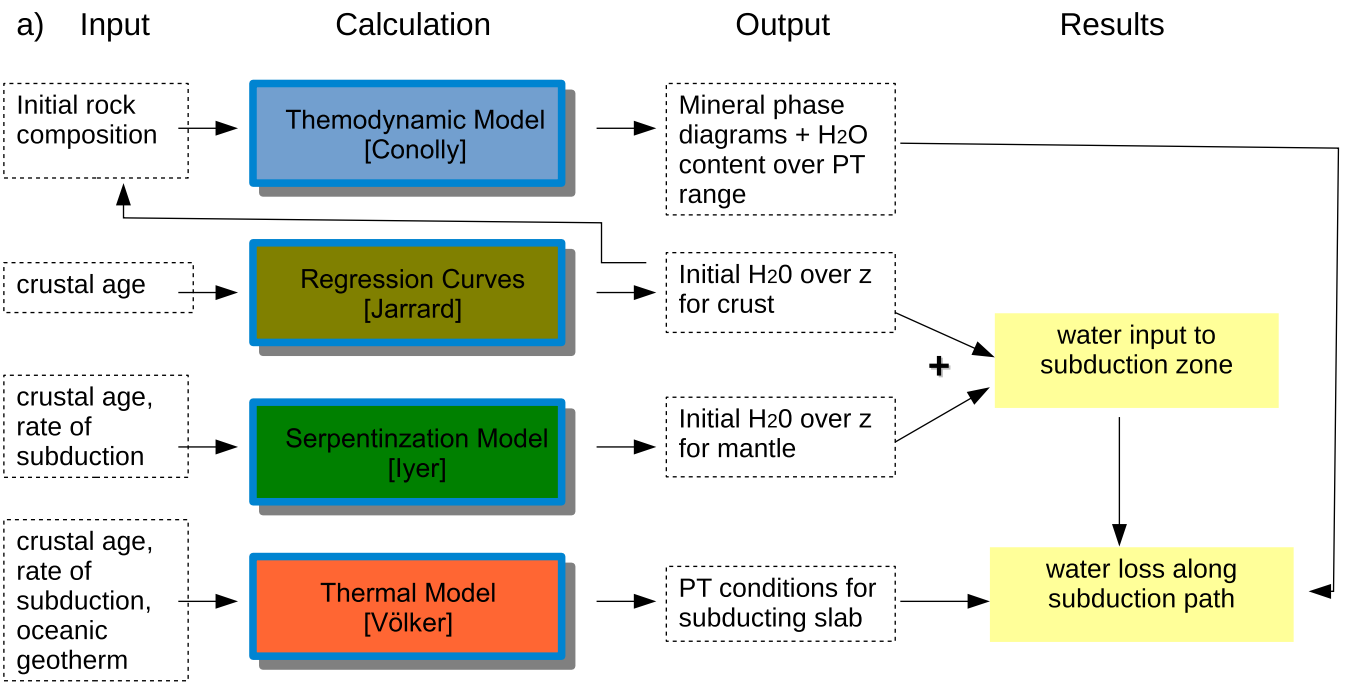

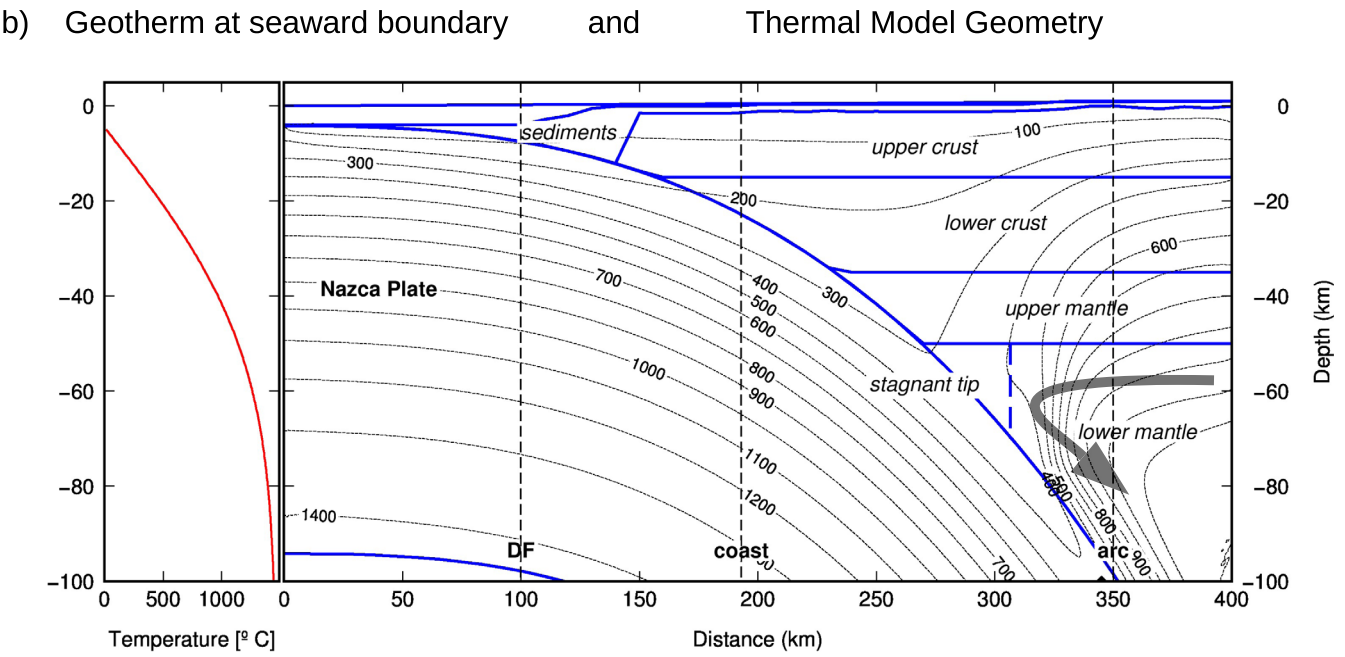

Figure 2. (a) Work flow and interplay of calculations and models used in this study. (b) Sample input (geothermal profile at the ocean boundary) and model space of thermal 2-D finite element model. The gray arrow symbolizes flow in the continental mantle; DF = deformation front.

present at this stage, they represent the final mineral phases containing stochiometric water [*Lippard et al.*, 1986; *Bucher and Frey*, 2002]. They are decomposed below 800°C.

4. Methodology

4.1. Work Flow

The work flow is illustrated by Figure 2a. It consists of (1) calculating phase diagrams for relevant water-bearing minerals over the range of PT conditions of subduction zones with Perple_X [*Connolly*, 2009,

version 6.6.9 with thermodynamic data file hp02ver.dat], (2) calculating the water content of oceanic crust according to *Jarrard* [2003], including both pore water and structural water (mineralogically bound water), (3) calculating the water uptake of the oceanic mantle due to serpentinization with a numerical model of *Iyer et al*. [2012], (4) producing grids of PT conditions for the subducting slab with a thermal finite element model according to *Völker et al*. [2011a, 2011b], and (5) calculating the water loss of the slab along the path of subduction by combining (1)–(4).

4.2. Phase Diagrams

Phase diagrams of the crustal and mantle rocks, their water-releasing reactions and the remaining water in the slab were calculated with Perple_X [*Connolly*, 2009] for a pressure range of 0.5–5 GPa and a temperature range of 100–1000°C. We calculate mineral reactions that change the water content of the subducting oceanic crust, based on a bulk major element composition of metabasalt compiled by *Staudigel et al*. [1996] and by *Connolly* [1990, Table 2]. Both compositions yield similar phase diagrams. In order to account for water-rich mineral phases that form in the uppermost oceanic crust, we follow the concept of *Jarrard* [2003] of dividing the crust into four layers (top extrusives, bottom extrusives, dikes, and gabbros) of 300, 300, 1400, and up to 5000 m thickness with different water content and thus different mineral phases. With respect to the phase diagrams, however, the upper two layers (0–600 m, extrusive layers 1 and 2 of *Jarrard* [2003]) behave sufficiently similar that we combine them into a single unit with a mean water content of 7.5–7.9 wt % H_2O. Similarly, phase reactions of the lower two crustal layers (dikes and gabbros) can be represented by a single composition with a water content of 1.6 wt % H_2O. Accordingly, the initial crustal composition used to calculate the phase diagrams is generated by adapting the metabasalt composition of *Staudigel et al*. [1996] to mean water contents of 1.60 and 7.67 wt % for the lower and upper layers of the crust, respectively (Table 2). This simplification is justified, as a finer subdivision in terms of phase reactions does not significantly change budgets and water release curves (see supporting information Figure S1). Phase diagrams of the mantle rocks and the corresponding remaining percentage of water are calculated based on the composition of serpentinized harzburgite of *Kerrick and Connolly* [1998, Table 2] or serpentinite [*Hacker et al*., 2003a].

4.3. Initial Water Content of the Oceanic Crust

For the calculation of the initial water input of the subducting oceanic crust, we follow the full four-layer concept of *Jarrard* [2003] in distinguishing between top extrusives, bottom extrusives, dikes, and gabbros. Based on measurement on DSDP and ODP drill cores, *Jarrard* [2003] documents the age dependency of density, porosity, and bound water content of the extrusive layers. We combine the regression curves of *Jarrard* [2003] with global mean values of matrix density and porosity of the lower layers to calculate the total water content of the crust (Table 3). We then multiply this crustal water content with the plate convergence rate to get the flux of crustal water over the five Nazca Plate segments of different age. We adapted the thickness of the gabbroid layer to the observed crustal thickness off Southern Central Chile (5–6 km) [*Scherwath et al*., 2009; *Contreras-Reyes et al*., 2007]. The top extrusives of the youngest crust segment are the most porous layer and carries up to 9.58 wt % of water, the bottom extrusives contain up to 6.17 wt % of water (Table 3). Below the extrusives ($z > 600$ m), the water content is significantly lower (2.84 and 1.03 wt %, Table 3). The total mass of water subducted with the crust over the 1480 km long SVZ is roughly 1000 kg/s (Table 3).

4.4. Water Uptake at the Outer Rise by Upper Mantle Serpentinization

Most models of mantle serpentinization assume that the mantle is homogeneously serpentinized to some depth below the Moho, based on phase-equilibria [e.g., *Schmidt and Poli*, 1998; *Hacker et al*., 2003b; *Rüpke et al*., 2004; *Skelton et al*., 2005]. Here we use a new model proposed by *Iyer et al*. [2012], which accounts for the reaction rate of serpentine formation and for the dependency of the reaction on the availability of fluids. The model consists of a porous flow solver and is coupled to the serpentinization reaction via the mass conservation equation (consumption of fluid during the reaction) and the energy equation (exothermic heat of reaction). The initiation and growth of bending-related faults at the outer rise is simulated by assuming a linear increase in porosity toward the trench [*Iyer et al*., 2012], thereby determining the amount of fluid available for the reaction. Downward fluid flow initiates as porosity opens due to progressive faulting toward the trench and is sustained by the consumption of fluid at depth due to serpentinization [e.g., *Lefeldt et al*., 2012]. However, vigorous hydrothermal convection does not occur due to the relatively low

AGU Geochemistry, Geophysics, Geosystems 10.1002/2015GC005766

Table 3. Water Content of the Subducting Nazca Plate Crustal Layers of the Five Segments Defined in Table 1[a]

	Name of Layer (m)	Thickness (m)	Matrix Density (kg/m^3)	Bulk Density (kg/m^3)	Macroporosity (%)	Microporosity (%)	Total Porosity (%)	Structural Water (wt %)	Pore Water (wt %)	Total Water Content (wt %)	Total Water Content (a) (g/m^3)	Total Water Content (b) (g/m^2)	Subducted Water (g/m/s)	Subducted Water Per Segment (g/s)
Water in the Subducted Crust After Jarrard [2003]														
Segment 1, North of Mocha FZ, 33°S–38°S, 580 km														
Layer 1	Top of extrusives	300	2914.84	2678.79	4.68	7.80	12.48	4.62	4.77	9.40	2.517E+05	7.551E+07	1.580E-01	9.166E+04
Layer 2	Bottom extrusives	300	2961.42	2817.24	2.34	5.10	7.44	3.43	2.70	6.13	1.727E+05	5.181E+07	1.084E-01	6.290E+04
Layer 3	Dykes	1400	2980.00	2920.54	0.84	2.20	3.04	1.76	1.07	2.83	8.253E+04	1.155E+08	2.418E-01	1.403E+05
Layer 4	Gabbros	3000	2990.00	2976.24	0.00	0.70	0.70	0.79	0.24	1.03	3.068E+04	9.204E+07	1.926E-01	1.117E+05
											Sum over all layers:	3.349E+8	7.009E-1	4.065E+5
Segment 2, Between Mocha FZ and Valdivia FZ, 38°S–40°S, 225 km														
Layer 1	Top of extrusives	300	2919.83	2542.44	5.13	7.80	12.93	4.38	5.21	9.58	2.437E+05	7.310E+07	1.530E-01	3.442E+04
Layer 2	Bottom extrusives	300	2963.92	2736.82	2.56	5.10	7.66	3.30	2.87	6.17	1.689E+05	5.066E+07	1.060E-01	2.386E+04
Layer 3	Dykes	1400	2980.00	2889.44	0.84	2.20	3.04	1.76	1.08	2.84	8.198E+04	1.148E+08	2.402E-01	5.405E+04
Layer 4	Gabbros	3000	2990.00	2969.08	0.00	0.70	0.70	0.79	0.24	1.03	3.062E+04	9.187E+07	1.923E-01	4.326E+04
											Sum over all layers:	3.304E+8	6.915E-1	1.556E+5
Segment 3, Between Valdivia FZ and Chiloé FZ, 40°S–41.5°S, 170 km														
Layer 1	Top of extrusives	300	2929.92	2524.86	6.03	7.80	13.83	3.88	5.61	9.49	2.395E+05	7.186E+07	1.504E-01	2.557E+04
Layer 2	Bottom extrusives	300	2968.96	2728.11	3.01	5.10	8.11	3.05	3.05	6.10	1.664E+05	4.992E+07	1.045E-01	1.776E+04
Layer 3	Dykes	1400	2980.00	2889.44	0.84	2.20	3.04	1.76	1.08	2.84	8.198E+04	1.148E+08	2.402E-01	4.084E+04
Layer 4	Gabbros	3000	2990.00	2969.08	0.00	0.70	0.70	0.79	0.24	1.03	3.062E+04	9.187E+07	1.923E-01	3.269E+04
											Sum over all layers:	3.284E+08	6.873E-01	1.168E+05
Segment 4, Between Chiloé FZ and Guafo FZ, 41.5°S–43.5°S, 225 km														
Layer 1	Top of extrusives	300	2938.82	2509.18	6.82	7.80	14.62	3.44	5.97	9.41	2.360E+05	7.081E+07	1.482E-01	3.334E+04
Layer 2	Bottom extrusives	300	2973.41	2720.39	3.41	5.10	8.51	2.83	3.20	6.04	1.642E+05	4.927E+07	1.031E-01	2.320E+04
Layer 3	Dykes	1400	2980.00	2889.44	0.84	2.20	3.04	1.76	1.08	2.84	8.198E+04	1.148E+08	2.402E-01	5.405E+04
Layer 4	Gabbros	3000	2990.00	2969.08	0.00	0.70	0.70	0.79	0.24	1.03	3.062E+04	9.187E+07	1.923E-01	4.326E+04
											Sum over all layers:	3.267E+08	6.838E-01	1.539E+05
Segment 5, South of Guafo FZ, 43.5°S–46°S, 280 km														
Layer 1	Top of extrusives	300	2970.03	2453.11	9.61	7.80	17.41	1.90	7.27	9.16	2.248E+05	6.743E+07	1.411E-01	3.951E+04
Layer 2	Bottom extrusives	300	2989.01	2693.05	4.81	5.10	9.91	2.06	3.77	5.83	1.569E+05	4.708E+07	9.854E-02	2.759E+04
Layer 3	Dykes	1400	2980.00	2889.44	0.84	2.20	3.04	1.76	1.08	2.84	8.198E+04	1.148E+08	2.402E-01	6.726E+04
Layer 4	Gabbros	3000	2990.00	2969.08	0.00	0.70	0.70	0.79	0.24	1.03	3.062E+04	9.187E+07	1.923E-01	5.384E+04
											Sum over all layers:	3.212E+08	6.721E-01	1.882E+05
Total subducted water over the SVZ													Sum over all segments:	1.02E+006

[a]The total water content (b) is the volume of water that is stored in a crustal column of 1 × 1 m dimensions over the depth of the layers. The subducted water is this amount multiplied by the rate of subduction. The subducted water per segment is the subducted water per 1 m of subduction zone length multiplied with the length of the subduction zone segment.

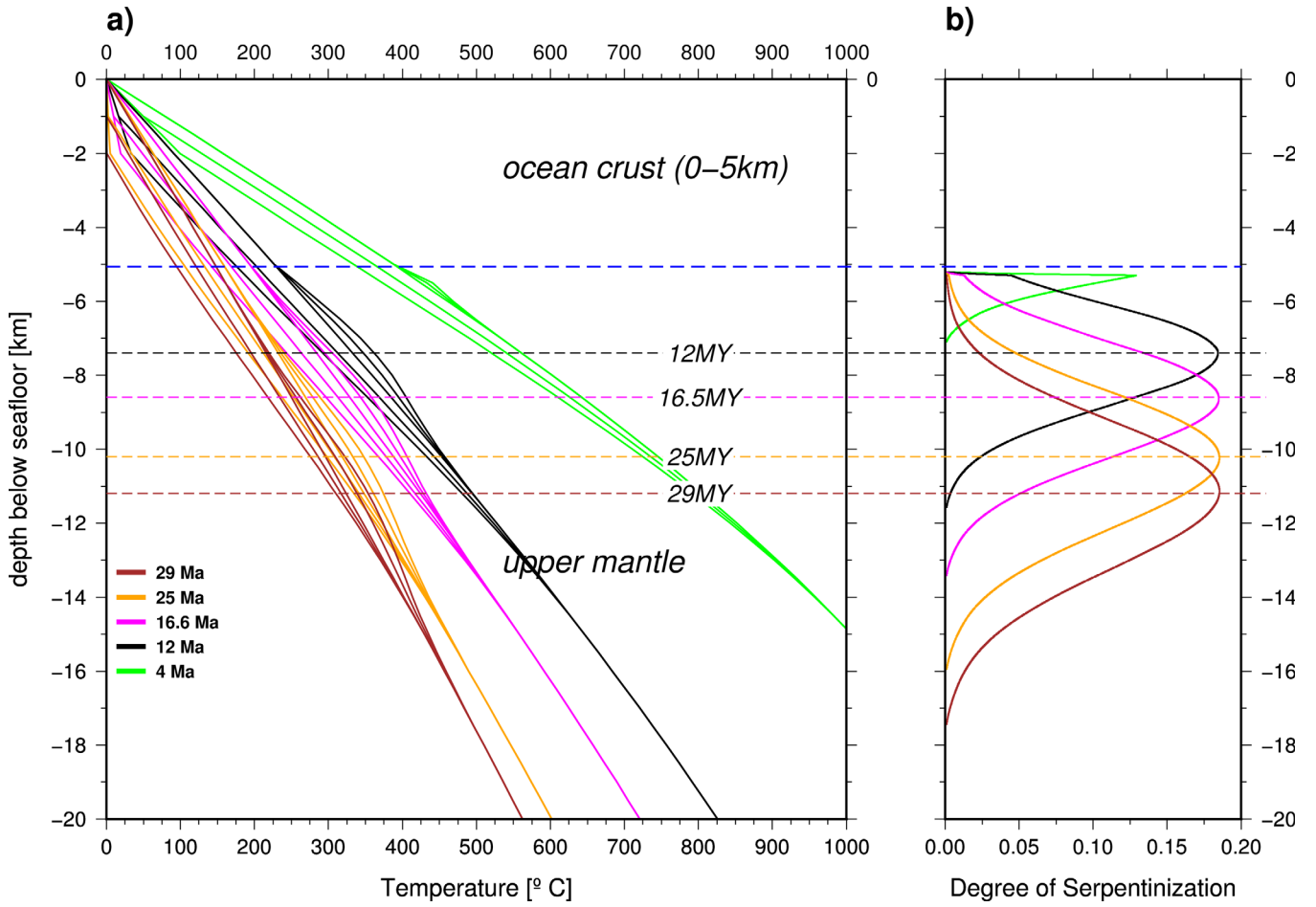

Figure 3. (a) Geothermal gradients at the outer rise for five age segments of the Nazca Plate, based on the half-space cooling model of *Stein* and *Stein* [1992]. The half-space cooling model geothermal gradient is modified to simulate the exothermic serpentine reaction effect and the effect of crustal cooling by seawater percolation. The serpentine reaction effect adds a maximum of 30°C and is restricted to the depth interval of serpentinization (Figure 3b). Seawater percolation lowers crustal temperatures over the depth interval of intense seawater percolation, but also lowers the upper plate temperature for the GDH1 model. (b) Degree of serpentinization of the upper oceanic mantle at the outer rise against depth, according to the model of *Iyer et al*. [2012]. The maximum of serpentinization is found at the 270°C isotherm.

permeability and low thermal gradients. Serpentinization occurs in a band-like pattern dictated by the reaction kinetics.

The rate of serpentinization is derived from experiments [*Martin and Fyfe*, 1970; *Wegner and Ernst*, 1983; *Malvoisin et al*., 2012] and shows a strong temperature dependency. This dependency is described by a bell-shaped curve with a peak reaction rate at 270°C and essentially no reaction occurring below 100°C and above 400°C (Figure 3b). The reaction rate also depends on the amount of fluid present. The modeled domain consists of an across-trench 2-D slice of the lithosphere extending 120 km seaward of the trench and 75 km deep. Temperature in the model is initialized by the plate cooling model GDH1 [*Stein and Stein*, 1992] for the given plate age. Oceanic mantle enters the domain at the subduction velocity and becomes serpentinized. Local spatial variability in the fracture distribution cannot be considered as required input data are not available. The model time is the period to move the lithosphere 120 km from the outer rise to the trench. A complete description of the model, the governing equations and parameters are given in *Iyer et al*. [2012].

We used this model to calculate the initial profile of serpentinite content in the mantle for each of the segments before being subducted. The initial degree of mantle serpentinization s is converted into water content of the mantle in kg/m^3, given that a fully serpentinized mantle contains 13 wt % of water [*Schmidt and Poli*, 1998]. Thus, $m(H_2O) = s * 13/100 * \rho$ (serpentinized mantle) with ρ(serpentinized mantle) $= (1 - s) * \rho$ (peridotite) $+ s * \rho$ (serpentine) assuming ρ (peridotite) $= 3300$ kg/m^3 and ρ (serpentine) $= 2600$ kg/m^3.

Table 4. Water Input Flux With the Subducting Mantle

Segment	Depth of Maximum Serpentinization (km)	Water Content (g/m^2)	Water Content Per Segment (g/m)	Input Flux (g/m/s)
Water Input Flux With the Subducting Hydrated Mantle				
North of Mocha FZ, 33°S–38°S	11.1	3.83E+08	2.22E+14	8.02E-01
Between Mocha FZ and Valdivia FZ, 38°S–40°S	10.2	3.52E+08	7.91E+13	7.36E-01
Between Valdivia FZ and Chiloé FZ, 40°S–41.5°S	8.6	2.94E+08	5.00E+13	6.15E-01
Between Chiloé FZ and Guafo FZ, 41.5°S–43.5°S	7.4	2.46E+08	5.52E+13	5.14E-01
South of Guafo FZ, 43.5°S–46°S	5.0	3.50E+07	9.81E+12	7.33E-02
Sum			4.17E+14	

Since the subduction velocity is the same for all plate segments, the depth profile of serpentinization is controlled exclusively by the thermal structure of the slab (Figure 3b). The amount of water taken up by serpentinization is calculated for each profile by integrating the water content in the mantle column at the trench. The water content in the mantle due to serpentinization increases northward, as the depth interval over which serpentinization takes place broadens due to increasing slab ages. The maximum water content is 76.4 kg/m^3 of rock, which is reached in four of the five segments (Figure 3b). Only for the hottest segment 5, the 270°C isotherm, i.e., the depth at which maximum serpentinization occurs, is not located in the upper mantle, but above in the oceanic crust. The depth of the 270°C isotherm increases with plate age from 5.3 km (4 Ma) to 11.1 km (30 Ma). If we integrate over depth from the Moho downward, a column of 1 × 1 m slab contains from 3.5×10^4 kg (4 Ma) to 3.8×10^5 kg (30 Ma) of water (Table 4).

4.5. Description of the Thermal Model

The temperature field along trench-perpendicular profiles is created using the 2-D finite element code PGCtherm written by Jiangheng He (Pacific Geoscience Centre of the Geological Survey of Canada). The model profiles run from the Nazca Plate, 100 km seaward of the deformation front across the Chilean fore arc and arc and 50 km into the Argentinean back arc (Figure 2b). The code was used before for geothermal models of subduction zones around the world [*Currie et al*., 2004; *Wada et al*., 2008; *van Keken et al*., 2008; *Wada and Wang*, 2009; *Völker et al*., 2011a].

The model space is discretized into layers that represent sediments, upper continental crust, lower continental crust, lithospheric continental mantle, asthenospheric continental mantle as well as the subducting oceanic slab. The main boundary conditions of the model consist in the prescribed motion of the subducting plate and defined vertical temperature profiles at the seaward boundary and at the landward boundary (back arc).

The geometry of the plate interface has been constrained by wide-angle seismic data to ∼100 km depth [*Scherwath et al*., 2009; *Contreras-Reyes et al*., 2008] and by Wadati-Benioff seismicity of local seismic networks [*Bohm et al*., 2002; *Haberland et al*., 2006; *Lange et al*., 2007] for two model profiles at 38°S (Profile Mocha) and 42°S (profile Chiloé). The geometry of both profiles is similar with a slab dip of 4–5° at the trench, ∼15° below the coast, 23–30° below the fore arc and a slab depth of ∼100 km below the arc. To bridge the gap between these profiles, we calculated intermediate profiles with a geometry similar to the northern profile (Figure 4). The continental Moho is taken as a horizontal boundary at 35 km depth in agreement with thermal models of subduction zones of *Currie et al*. [2002, 2004] (Figure 2b).

In the asthenospheric continental mantle wedge (below 50 km) mantle flow is permitted. *Wada and Wang* [2009] show that at most subduction zones the downgoing slab is mechanically decoupled from the continental mantle to a depth of 70–80 km. As the coupling between the plates drives the flow within the viscous mantle wedge, this leads to the effect that mantle flow does not extend into the mantle wedge tip (Figure 2b). *Wada et al*. [2008] also showed that the (vertical) transition from stagnant to flowing parts of the viscous mantle wedge is sharp. We therefore follow *Peacock and Wang* [1999] and *Currie et al*. [2004] in imposing a nonflow condition to the tip of the mantle wedge. The vertical, landward boundary of this nonflow zone is located where the plate interface is 70 km deep (Figure 2b).

Radiogenic heat production within the continental crust is accounted for by prescribing a higher value (1.3 $\mu W/m^3$) for the upper and a lower value (0.4 $\mu W/m^3$) to the lower crust, with a division at 15 km depth.

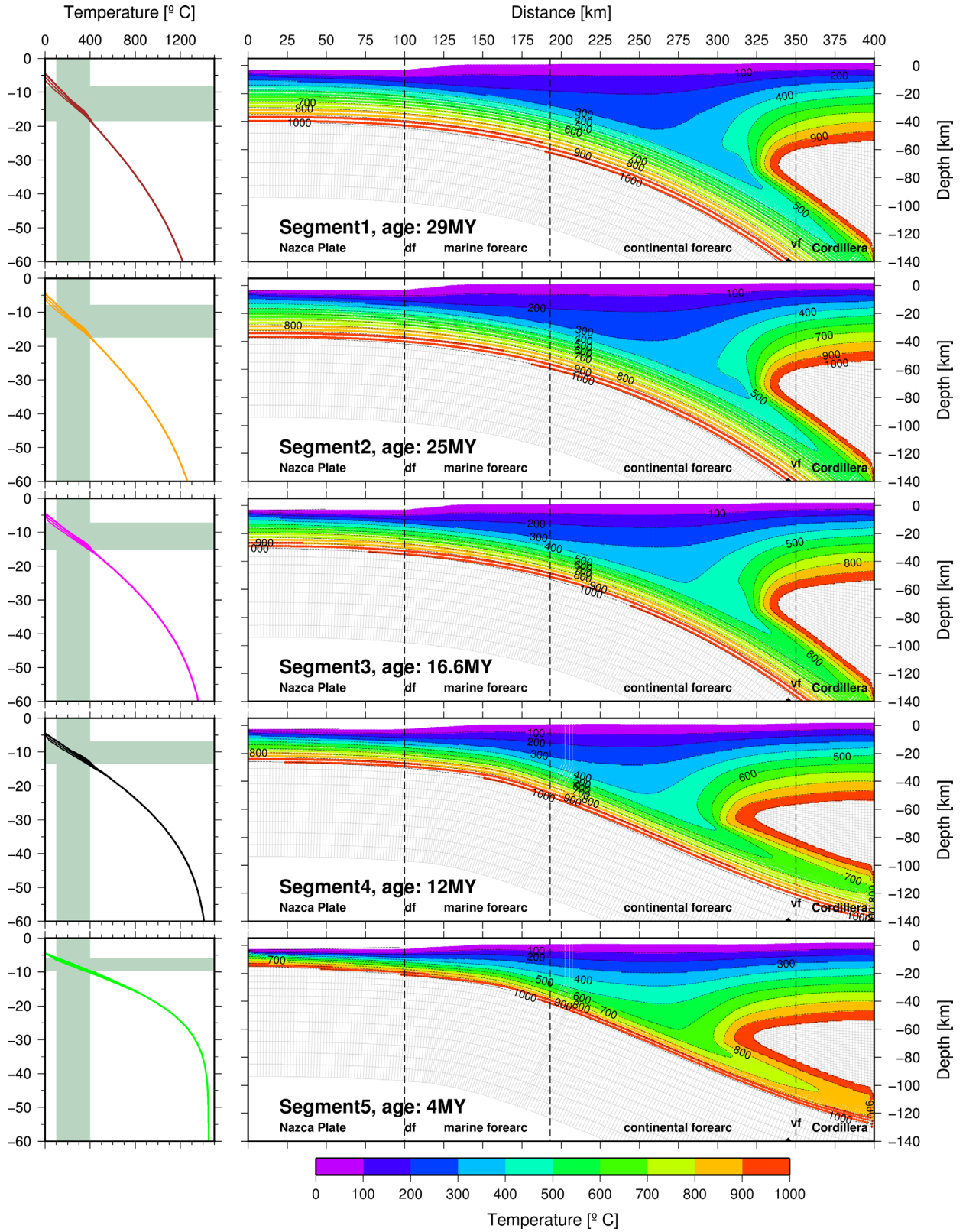

Figure 4. Thermal models of the Chile Subduction Zone (right column) and geothermal gradient at the ocean boundary (left column; $z = 0$ corresponds to the seafloor) for the five age segments of the Nazca Plate (Figure1) from 100 km seaward of the deformation front to the back arc. Greenish zones in the temperature depth curves depict the temperature/depth window for mantle serpentinization at the outer rise; df = deformation front, vf = volcanic front of the Andes.

Frictional heating along the plate interface is an extra heat source. In the brittle region, the shear stress τ along the interface is governed by the static friction law $\tau = \mu' \sigma_n$, where μ' is the effective coefficient of friction that accounts for the effects of pore fluid pressure [*Wang and He*, 2008], and σ_n is the normal stress acting on the plate interface. The latter is approximated by an integration of rock density over depth. The rate of heat generation per unit fault area is $Q_f = \tau v$, where v is the sliding velocity. We apply a low effective coefficient of friction of 0.03–0.05 in accordance with *Wang and Hu* [2006], *Wang and He* [2008], and *Harris et al*. [2010], resulting in a maximum shear stress of 34–56 MPa along the plate interface. The continental mantle is generally considered hydrated allowing for continuous ductile deformation of especially serpentine and other hydrated mineral phases. Therefore, tectonic loading can continuously be released and the continental mantle is too weak to produce significant friction along the plate interface [*Currie et al*., 2002].

The basic geothermal gradient at the ocean boundary of the model is calculated using the GDH1 model [*Stein and Stein*, 1992] with the temperature T as a function of plate age t and depth z given by:

$$T(t,z) = T_m \, erf\left(z/\sqrt{4\kappa t}\right) \quad (1)$$

where $T_m = 1450°C$. Here $\kappa = k/(\rho c)$ is the thermal diffusivity, with $c = 1171$ J/kg, $k = 3.138$ W/m/K, and $\rho = 3330$ kg/m^3. We then modify this basic geothermal gradient as follows: (1) we simulate the exothermic effect of serpentinization by adding a "serpentine reaction effect" that raises the oceanic mantle temperature over the depth interval of serpentinization; (2) we simulate the cooling effect of seawater percolation to a depth of some km; and (3) we combine both effects. The serpentine reaction effect is related to the depth distribution of serpentinization and leads to a maximum temperature increase of 30°C [see *Iyer et al*., 2012, Figure 3a]. The seawater cooling effect lowers the geothermal gradient primarily over the prescribed depth of intense water percolation z_p, but the effect extends to greater depth. In the most extreme, theoretically possible case, the temperature of the oceanic crust is set to water temperature (0°C) from the seafloor down to the assumed depth of percolation z_p, while the geothermal gradient from z_p downward is calculated according to the GDH1 model, (taking z_p as z in equation (1)). As this case would require unrealistically high crustal permeabilities, we use an intermediate approach by (1) calculating the GDH1 gradient from z to z_p for the different crustal segments, (2) reducing that gradient (by up to 0.5) over the supposed depth of percolation, and (3) fitting the gradient below z_p to the reduced upper plate temperature (Figure 3a). The maximum temperature reduction relative to a standard GDH1 model is in the range of 25–60°C in the cooled depth interval.

The geothermal gradient at the continental boundary of the model must fit the limited heat flow data of the back-arc region (Patagonian Platform) of 74 m W m^{-2} [*Hamza and Munoz*, 1996]. Its implementation follows the model of *Rudnick et al*. [1998] and *Jaupart and Mareschal* [1999].

4.6. Calculation of Water Release From the Oceanic Crust and Mantle

We calculate the volumes of water released from the slab along the subduction path by (I) calculating PT conditions for the subducting slab (with the FE model described in section 4.5), (II) imposing the water content of the slab at the seaward (outer rise) model boundary (initial water content of the crust, section 4.3 and water uptake of the mantle, section 4.4), (III) mapping the PT conditions along the subduction path onto stability fields of the relevant water-bearing minerals. The stability fields are directly related to percentages of remaining water, which allows (IV) to calculate the remaining (respectively the released) water volumes. A similar scheme was used by *van Keken et al*. [2011] in a global compilation. The water release is calculated separately for upper crust, lower crust, and upper mantle as described in section 4.2. The total water release is the sum of the water release from those reservoirs.

PT conditions of the subducting slab are calculated and exported as lists of nodes with their position, pressure, and temperature. Then, the nodes of the FEM grid with the initial water content are tracked within the PT grid of mineral stability. Each point in the grid is attributed a percentage of remaining water, depending on PT conditions. Using these results, we calculate the released water from the coast to the volcanic front by integrating the water content over all depths at a given position.

5. Results

Our modeling results clearly show the impact of plate age on water uptake and water release/retention for both subducting oceanic crust and upper mantle. The amount of water that is carried into the subduction

zone with the oceanic crust is relatively constant over the working area. In contrast, the volume of water carried by upper oceanic mantle varies by one order of magnitude.

5.1. Water Storage in, and Water Release From the Crust

Thirty-six to thirty-eight percent of water that is absorbed by the oceanic crust prior to subduction is stored in the 600 m thick extrusive layers. The lower part of the crust (4400 m of dikes and gabbros, in the case of Chile) carries the remaining 62–64%. Porosity decrease with age in the extrusive layers is counteracted by increasing basalt alteration with age (leading to an increase of water content) in a way that the water content of the total crust varies little over the working area. The influx of water within the oceanic crust amounts to 0.67–0.71 g/m of subduction zone per second (Table 3). The release of water from the crust is primarily temperature-dependent and starts to become important at temperatures exceeding 250–300°C for the water-rich extrusive layers 1 and 2 (Figure 5a) and above 500°C for the water-poor gabbros and dikes of the lower crust (Figure 5b).

5.1.1. Upper Layers of the Crust (0–600 m)

The most important water-releasing mineral phase transitions in the top extrusive layers are related to the breakdown of the zeolite minerals, analcite and pumpellyite, and these reactions occur at and below 300°C and 0.6–0.8 GPa (Figure 5a). For a high geothermal gradient (hot subduction zone), the decomposition of various phyllosilicates, epidote, and actinolite occurs over a temperature range of 300–500°C and continuously produces water at pressures of 0.8–1.1 GPa. For cold subduction, the decomposition of tremolite, chlorite, paragonite, and lawsonite releases significant amounts of water at blueschist facies conditions below 500°C and 1.8 GPa (Figure 5a). The breakdown of glaucophane and paragonite and—under low temperature eclogite conditions of fast subduction—the breakdown of zoisite and talc produce only little water over a relatively wide pressure and temperature range.

Consequently, gradual upper crustal dewatering is expected where the topmost 600 m of the subducting slab pass the temperature range between 300 and 600°C (Figure 5a). These conditions are met under the continental fore arc (Central Valley of Chile) and volcanic arc (x = 280–300 km in Figure 4c) for the relatively old slab north of 40°S (plate age of 25 and 29 Ma, Figure 4a, orange and brown PT path, segments 1 and 2) but dewatering is not fully accomplished under the arc. Therefore, a large fraction of that water (38% of the upper crustal water for 29 Ma old crust, 37% for 25 Ma old crust, and 31% for 16.6 Ma old crust) is carried into the back arc (Figures 5a and 5c). For younger slab age, south of 42°S (segments 4 and 5), the dewatering sets in earlier underneath the marine and continental fore arc (black and green lines in Figures 5a and 5c). The process of crustal dewatering is not instantaneous, but stretches over some 60–80 km in direction perpendicular to the trench, as the mineral reactions involved allow for a progressive water release (Figures 5a and 5c). For the youngest two segments (4 and 5), the dewatering of the uppermost layers of the crust is far progressed underneath the Cordillera (remaining upper crustal water of 13% for 12 Ma old crust). The upper layers of the youngest and hottest segment 5 (4 Ma) begins to loose water under the marine fore arc and becomes relatively dry under the continental fore arc (remaining upper crustal water of 3%, green line in Figures 5a and 5c).

The exact location of the initiation of the upper crust dewatering is sensitive to the décollement temperature, which in turn is dependent on assumptions on the temperature gradient at the ocean boundary of the model and on frictional parameters at the plate contact. In our models, we assume conservative (low) values for the effective coefficient of friction.

5.1.2. Lower Layers of the Crust (600–5000 m)

The dehydration reactions of the lower layers of the crust (gabbros and dikes, according to *Jarrard* [2003]) differ significantly from those of the upper layers due to the lower initial water content. Hence, different phase-equilibria are required (Figure 5b), characterized by little dewatering at temperatures below ~550°C and rather instantaneous dewatering at higher temperatures, due to the breakdown of lawsonite, glaucophane, actinolithe (and other Na-Ca-amphiboles), chlorite, and zoisite.

Only in the case of the youngest and southernmost Nazca Plate segment (segment 5), the lower portions of the crust encounter these high temperatures under the continental fore arc (Figure 5b, green line) at x = 240 km (Figure 5c). This segment consequently loses most of the water carried in the lower part of the crust while only 14% of it enters the back arc. The segment north of it (segment 4, 12 Ma) is affected by dehydration of the lower portions of the crust just below the Cordillera (Figures 5b and 5c, black line) but

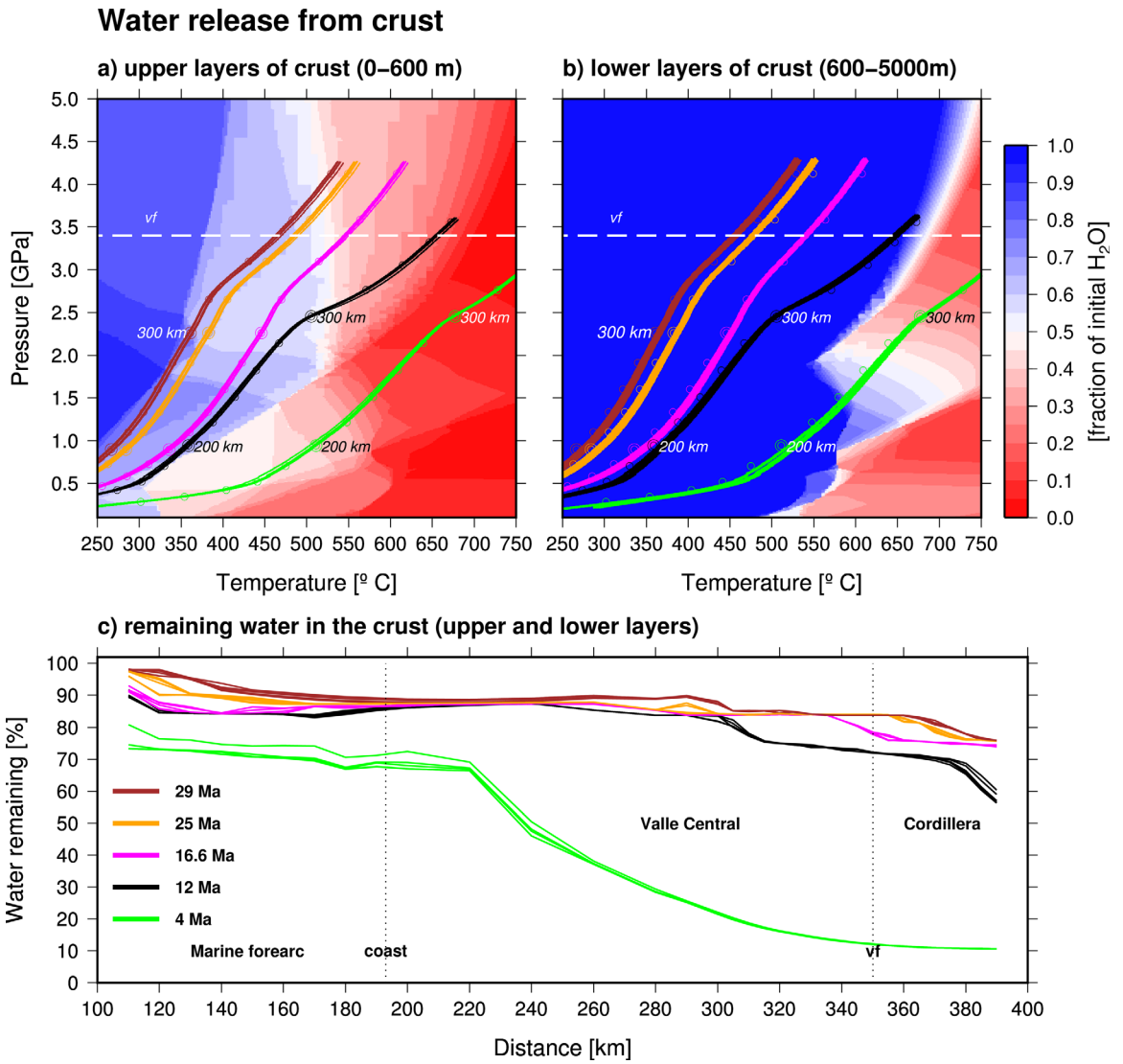

Figure 5. Water release and water retention for five segments of the subducting oceanic crust: (a) Remaining percentage of water for water-rich metabasalt (upper layer of the oceanic crust, 7.6 wt % H_2O, Table 2) over the PT range to a depth of 120 km. Colored lines display PT conditions along the subduction path for the uppermost crust for the five segments and a set of starting conditions (Figure 3a). The *x* coordinates along the subduction path are indicated as points in 20 km intervals. (b) Remaining percentage of water for water-poor gabbros (lower portion of the oceanic crust, 1.6 wt % H_2O, Table 2). Colored lines display PT conditions of the subducting upper crust for four segments of the Nazca Plate. (c) Percentage of the incoming water that is released from the crust (upper and lower portion) over the fore arc or, alternatively, transported into the back arc. Lines of the same color represent the range of variation due to modifications of the geothermal gradient at the ocean boundary (Figure 3a). The *x* axis corresponds to Figures 2b and 4, accordingly the profile stretches from the continental fore arc (Central Valley of Chile) to the volcanic arc.

still keeps 79% of its initial water content, whereas for all of the other segments, the lower crust is not affected by dewatering over the fore arc and arc.

5.2. Water Storage in and Water Release From the Upper Serpentinized Mantle

In contrast to the crust, where the topmost hundreds of meters have the highest water content, the serpentinized mantle carries water in a bell-shaped distribution over a wider depth interval around a maximum defined by the 270°C isotherm (Figure 3b and Table 4) [cf. *Iyer et al.*, 2012]. With increasing plate age, the depth of the maximum serpentinization moves deeper and a larger depth interval of the mantle gets involved. For the youngest segment (4 Ma), this bell-shaped curve is truncated as the uppermost mantle temperature exceeds 270°C (Figure 3b). Consequently oceanic mantle of our oldest segments carries roughly ten times more water into the subduction zone than the youngest segments (Table 4). The water

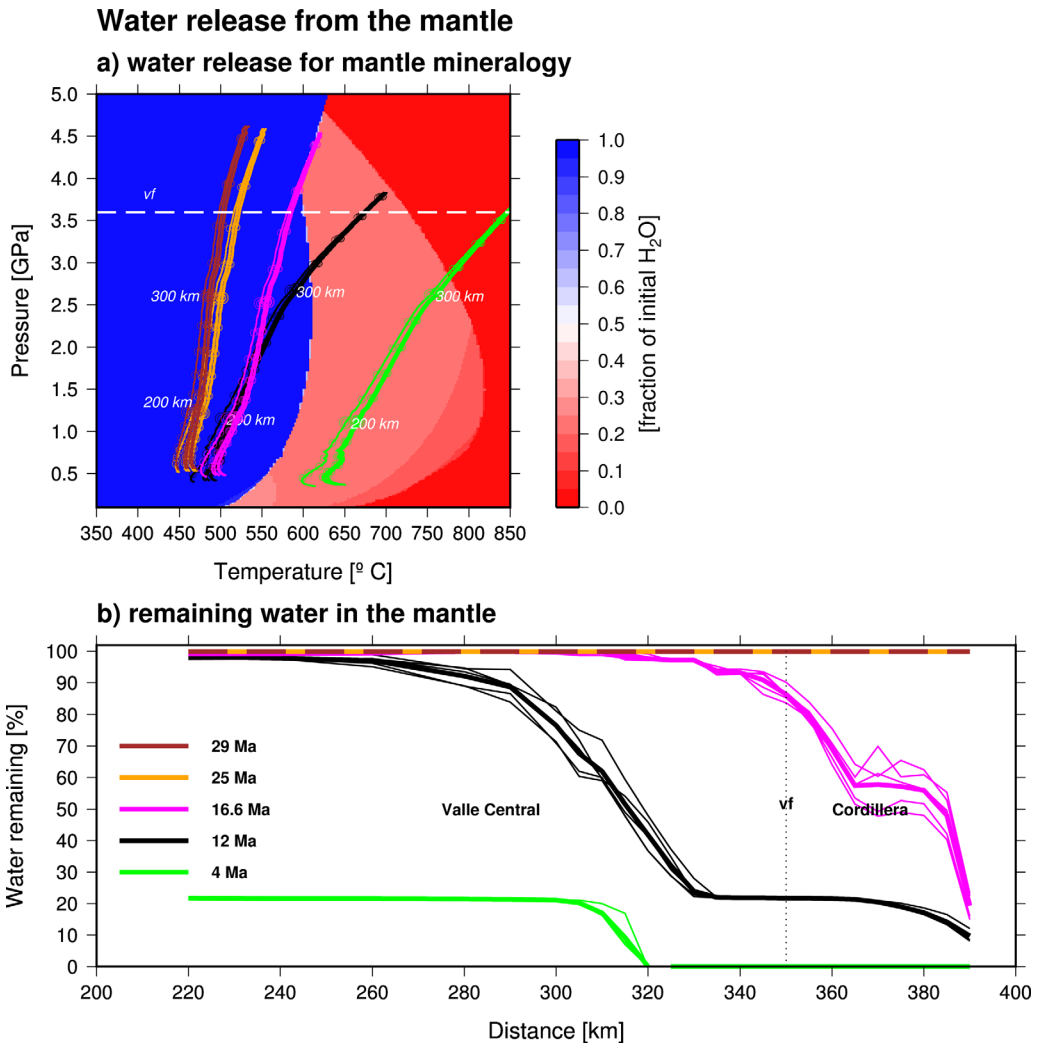

Figure 6. Water release and water retention for the five age segments of the subducting oceanic mantle: (a) Remaining percentage of water for serpentinized mantle (composition in Table 2) over the PT range of subduction to a depth of 120 km. Colored lines display the PT path of the subducting part of the mantle for five segments of the Nazca Plate, for different starting conditions (Figure 3a). The appended *x* distances relate to the profile distance. More specifically, the lines represent the PT paths of the depth level of maximum serpentinization (270°C isotherm at the outer rise, see Figure 3b). (b) Percentage of the incoming water that is released from the mantle over the fore arc or, alternatively, transported into the back arc for five Nazca Plate segments. Lines of the same color represent the range of variation due to modifications of the geothermal gradient at the ocean boundary (Figure 3a). The *x* axis corresponds to Figures 2b and 4, so this is a profile from the fore arc (Central Valley of Chile) to the volcanic arc.

input flux of the mantle for the oldest segment (29 Ma) is 0.8 g/m of the subduction zone per second, which is comparable to the water input of the crust (0.672 g/m/s), whereas the youngest mantle segment (4 Ma) brings in 0.073 g/m/s.

The process of water release from the mantle by deserpentinization starts at temperatures exceeding 500–550°C (Figure 6a) and happens in two steps that are related to the decomposition of antigorite and brucite (brucite out) and to the final breakdown of antigorite (antigorite out) at approximately 600°C. The PT paths of the subducting mantle at the respective depth of maximum serpentinization (colored lines in Figures 6a and 6b) remain in the stability field of serpentine minerals for the oldest two segments of the mantle (25 and 30 Ma, orange and black lines in Figure 6), therefore the water stored in the serpentinized mantle is carried into the back arc. The 17 Ma old mantle progressively dewaters under and behind the volcanic arc, as more and more of the serpentinized part of the mantle reaches PT conditions that activate dewatering reactions (magenta-colored line in Figure 6b). For the youngest two mantle segments, the mantle dewatering is largely completed below the fore arc (black and green lines in Figure 6b).

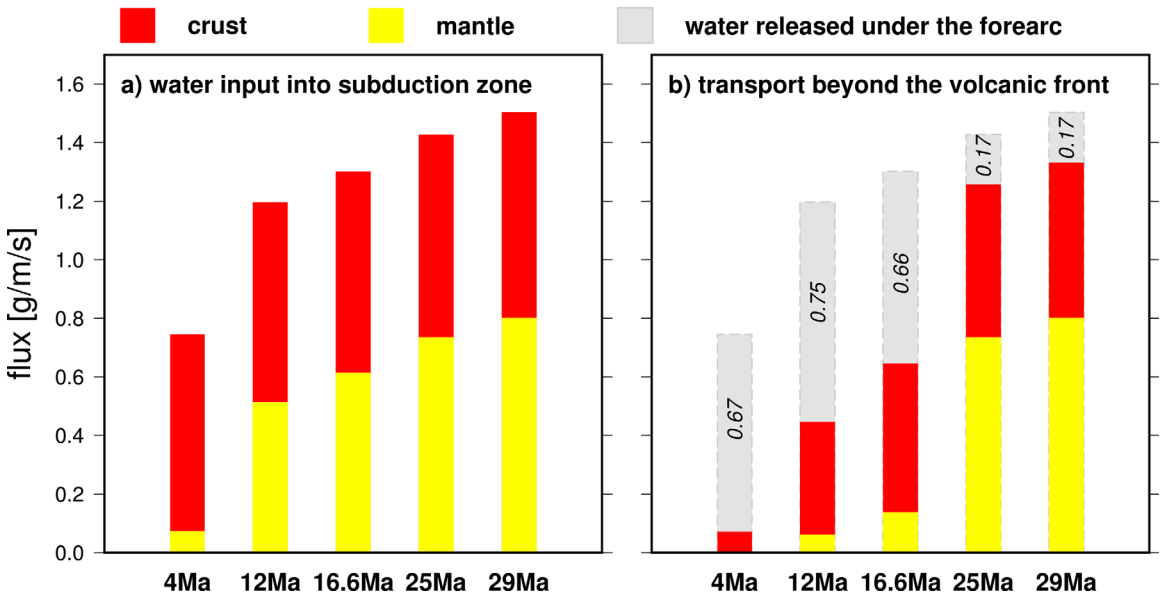

Figure 7. (a) Water influx into the subduction zone at the deformation front, 250 km west of the volcanic arc (initial water influx) for the five Nazca Plate segments, as compared to (b) water outflux at the end of the model profile, 50 km east of the volcanic arc. The difference between the cumulative bars of Figures 7a and 7b (gray bar) corresponds to the water that is driven out of the subducting slab under the fore arc.

6. Discussion

6.1. Budget of Water Uptake and Release

The volumes of water set free from the subducting oceanic slab under the fore arc depend on the thermal state of the subduction zone, which is related to the age of the oceanic crust. Two processes that predominantly determine these water volumes act as a counterbalance: (1) the water uptake by pore water storage, hydration of the crust, and mantle serpentinization at the outer rise and (2) the water-release from the upper and lower portions of the crust and the mantle under the fore arc by prograde metamorphic reactions. The water uptake by mantle serpentinization increases dramatically with the age of the plate because the depth interval of the mantle that can be affected by serpentinization extends. The crustal water uptake is age-dependent as well but to a much lesser degree (Figure 7a).

Water uptake may also be controlled by the intensity of bending-related faulting at the outer rise. In theory, young plate segments should have lower effective elastic thickness *Te* than older segments with the consequence that flexural faults, if even present, may not reach deep enough below the crust to strongly hydrate the mantle. This configuration would result in an age-dependent (N-S) decrease in the intensity and depth of outer rise flexural faulting and upper mantle hydration. The latter effect would add to and amplify to the southward decrease in mantle hydration caused by temperature-controlled narrowing of the mantle depth interval over which serpentinization can happen (as is described in section 4.4), and thus would accentuate the calculated N-S differences in water input into the subduction zone even more. However, *Contreras-Reyes and Osses* [2010], in a paper dedicated to variations in the lithospheric flexure of the Nazca Plate prior to subduction offshore Chile (18°S–45°S) find that (1) *Te* decreases systematically at the outer rise when the lithosphere is bent into the subduction zone and they link this phenomenon to pervasive and deep faulting and that (2) neither the initial values of *Te* nor its reduction when approaching the trench are strictly age-related. Also they show by seismic reflection data and *vp* reduction from seismic refraction studies that deep faulting at the outer rise is present both in northern as well as in southern Chile. The rather uniform occurrence of outer rise bend faults in bathymetric data [*Weinrebe and Hasert*, 2012] over most of the working area points into the same direction.

The release of incoming water from crust and mantle under the fore arc and arc is correlated with age: the hotter the subduction zone is, the sooner the water gets driven out and the higher is the proportion of water that is released under the fore arc and arc relative to the total amount of water carried into the

Table 5. Crust and Mantle Water Input Fluxes and Output Fluxes to (a) Beneath Fore Arc and Arc and (b) Beyond the Arc

	Input Flux			Released Under Arc and Fore Arc				Transported Beyond the Arc			
	With Crust	With Mantle	Total	From Crust	From Mantle	Total	Total in % of Influx	In Crust	In Mantle	Total	Total in % of Influx
Input and Output Fluxes for the Nazca Plate Segments Subducting Under southern Central Chile											
Segment 1, North of Mocha FZ, 33°S–38°S, 580 km	7.01E-01	8.02E-01	1.50E+00	1.70E-01	8.02E-04	1.70E-01	11.3	5.31E-01	8.02E-01	1.33E+00	88.7
Segment 2, Between Mocha FZ and Valdivia FZ, 38°S–40°S, 225 km	6.92E-01	7.36E-01	1.43E+00	1.68E-01	7.36E-04	1.69E-01	11.8	5.23E-01	7.35E-01	1.26E+00	88.2
Segment 3, Between Valdivia FZ and Chiloé FZ, 40°S–41.5°S, 170 km	6.87E-01	6.15E-01	1.30E+00	1.79E-01	4.77E-01	6.57E-01	50.4	5.08E-01	1.38E-01	6.46E-01	49.6
Segment 4, Between Chiloé FZ and Guafo FZ, 41.5°S–43.5°S, 225 km	6.84E-01	5.14E-01	1.20E+00	2.99E-01	4.52E-01	7.51E-01	62.7	3.84E-01	6.22E-02	4.46E-01	37.3
Segment 5, South of Guafo FZ, 43.5°S–46°S, 280km	6.72E-01	7.33E-02	7.45E-01	6.01E-01	7.33E-02	6.74E-01	90.4	7.12E-02	0.00E+00	7.12E-02	9.6

subduction zone. This is true for upper and lower portions of the crust and for the mantle, but the water-releasing reactions in the crust are more complex and encompass a larger number of reactions over a wider PT range, whereas mantle dewatering occurs basically in two steps. It has been shown by *Wada et al*. [2012] that heterogeneities in the degree of hydration result in a shallower water release. At present, we can only state that presented depth ranges of water release in our study represent maximum values.

Integrated over the slab we get the intriguing result that the oldest Nazca Plate segment carries the largest mass of water into the subduction zone, but that little of that water is actually released under the fore arc and arc, whereas the hottest and youngest segment close to the Chile Triple Junction carries little water within the mantle but completely loses it under the fore arc (Figures 7a, 7b and Table 5). The conditions that in theory should be most appropriate for a high water flux to the fore arc and arc are met under relatively high but not the highest temperature conditions: a subduction zone that is cold enough for the mantle to become serpentinized over a large depth interval but hot enough to favor early water release under the fore arc. In the south-central Chilean subduction zone these conditions are met at segment 4 (12 Ma, 41.5–43.5°S, Figure 7b and Table 5). It releases 0.75 g/m/s of water to the fore arc, which is slightly more than the younger 4 Ma old segment 5 (0.67 g/m/s) and the older 16.6 Ma segment 3 (0.65 g/m/s). The oldest segments 1 and 2 with the largest water input release only 0.17 and 0.169 g/m/s of water to the fore arc (Figure 7b and Table 5). Hence, the interplay between age dependent water influx and release from three reservoirs control the water supply of the volcanic arc and fore arc along subduction zones.

The along-strike variations in the release of water from the subducting slab over a distance of ~1500 km are more prominent than expected and previously calculated. *van Keken et al*. [2011] distinguish three 490–640 km wide slab segments in the working area (centered around 30, 35, and 44°S) and calculate H_2O fluxes over depth of the slab. According to those calculations, the segments behave rather similar to a depth of 100 km (e.g., loss of 17%, 13%, and 19% of the water in a fully serpentinized case). Those trends are in general agreement with our results from the northern-central region of the working area, but do not resolve the high variability at its southern end approaching the Chile Rise where along-strike slab temperature gradients are the highest.

An indirect confirmation of the pattern of the latitudinal variations in fluid release under arc and fore arc presented here is found in variations in the geochemical signature of arc basalts of the SVZ of Chile. *Jacques et al*. [2014] report that isotope geochemistry of erupted arc basalts beneath the Chilean Central Southern Volcanic Zone (CSVZ, 38°S–43°S, corresponding to segments III and IV; Figure 1) reflect high fluid flux, much higher than further north beneath the Transitional Southern Volcanic Zone (TSVZ, 34.5°S–38°S, corresponding to segment I, Figure 1). It is also notable that the volumes of erupted material and estimated rates of magmatic production vary notably over the SVZ and that there is a peak at around 41°S (transition of segments II and III) as well as a decrease toward the northern and southern ends of the SVZ according to *Völker et al*. [2011b]. If the production of extruded magma is an indirect measure of fluid flux to the arc, then the general pattern fits.

The results show that variabilities in the pattern of water release over a single subduction zone can be in the same range than between subduction zones of very different character [e.g., *Jarrard*, 2003; *van Keken et al*., 2011]. In particular, the variability in the percentage of water that is released to the fore arc (11–90%

of the incoming water) is the same over the Chile Subduction Zone than is calculated globally between subduction zones [Table 2 of *van Keken et al*., 2011, comparison between input flux and flux at 100 km slab depth].

6.2. Potential Errors in Water Flux Estimation

Thanks to multidisciplinary research programs, namely the German Collaborative Research Centers SFB 574 ("Volatiles and Fluids in Subduction Zones"), SFB 267 ("Deformation Processes in the Andes"), SPOC ("Subduction Processes Offshore Chile"), and TIPTEQ ("From The Incoming Plate To MegaThrust EarthQuake Processes"), a number of geometrical and geochemical parameters of the Chilean subduction zone that impact on the water flux budget are relatively well constrained. This applies to the subduction geometry, the thickness of the incoming slab, constrained by wide-angle seismic [*Scherwath et al*., 2009; *Contreras-Reyes et al*., 2007], seismological [*Bohm et al*., 2002; *Haberland et al*., 2006; *Lange et al*., 2007] and gravimetric data sets [*Tassara et al*., 2006; *Alasonati-Tašárová*, 2007]. Also, some information on the initial serpentinization of the uppermost oceanic mantle at the outer rise is derived from v_p/v_s data [*Contreras-Reyes et al*., 2007]. These latter data only image the topmost few km of the oceanic mantle. Toward greater depth, however, when temperatures come close to 600–700°C serpentinization is largely negligible according to the stability of the serpentine minerals [e.g., *Evans et al*., 1976; *Wegner and Ernst*, 1983; *Ulmer and Trommsdorff*, 1995; *Wunder and Schreyer*, 1997].

We are, however, aware that some assumptions are not as well constrained by observations or are not testable. Some of these uncertainties could influence the modeling results of water release and water retention along the profiles, namely:

1. We The geothermal gradient of the ocean crust and mantle. This input parameter depends on the applied ocean plate cooling model and on assumptions regarding the thermal effect of the serpentine reaction as well as regarding crustal cooling due to seawater percolation. We have incorporated according variations by using a number of starting temperature models (see section 4.5), but these are based on assumptions, e.g., on the depth and intensity of seawater percolation that are poorly constrained. More sophisticated models of cooling by hydrothermal circulation in the oceanic crust have been presented recently by *Rotman* and *Spinelli* [2014] for Chile. The maximum temperature reduction in the crust that they predict to result from seawater influx lies in the upper range of our assumptions (e.g., a reduction by 55°C). Using different models of hydrothermal cooling shifts the foci of water release from the uppermost crust by some km.
2. The geometry of the subduction zone is quite well constrained by geophysical data as described by *Völker et al*. [2011a], but the uncertainty increases with distance from the trench. Reported differences in slab dip for the investigated zone of southern Central Chile are on the order of 5–7° [e.g., *Engdahl et al*., 1998; *Syracuse and Abers*, 2006; *Syracuse et al*., 2010]. Variations in the subduction angle lead to slightly different subduction paths through the PT field that in turn result in variations in the location of the maximum water release. This is particularly true if the dehydration happens stepwise like for the mantle (Figure 6a). Again, the largest effect would be on segment 3, as a slightly hotter PT path would release significantly larger amounts of water from the mantle under the fore arc (Figure 6a, magenta-colored line).
3. The mechanical nature of the slab/mantle-wedge interface is not fully understood but supposed to be very uniform for Nazca Plate subduction between 33°S and 46°S [cf. *Wada and Wang*, 2009]. The influence of decoupling on the thermal structure of the slab/mantle wedge interface remains a matter of debate [e.g., *Wada and Wang*, 2009; *Syracuse et al*., 2010]. It is likely that the decoupling depth is largely constant for the entire section along southern Central Chile and that variations in that depth can be neglected as effect on the slab temperature. However, a reliable quantification is missing.
4. The serpentinization of the oceanic mantle happens at the outer rise in our model. Inherited serpentinization and crustal hydration from the spreading ridge axis or fracture zones are not considered, because the intermediate to fast spreading at Chile Rise and Pacific-Farallon Spreading Center does not produce mantle exposures and intense detachment faulting allowing for direct mantle alteration at the seafloor or effective fluid circulation as it is the case for the slow-spreading scenario [e.g., *Cannat et al*., 2010]. In the case of southern Central Chile, outer rise faulting and alteration can be assumed to be most effective. Nevertheless, inherited serpentinization and crustal hydration prior to outer rise faulting could alter both

the total mass of subducted water and the depth interval of serpentinization. In that respect, the amount of water in our modeled crust and mantle is closer to a minimum than to a maximum estimate.

5. As the slab heats up, water is liberated from deeper levels of the downgoing plate and potentially rehydrates drier regions above. This effect should be most important for the northern colder segments, where more water is bound in deeper levels. For the total water budget however, we consider the effect as almost negligible because it should result merely in a slight delay of the water release. Hence, the amount of water released below the fore arc and arc could, if at all, be slightly reduced and our calculated amounts of water in crust and mantle would thus be rather minimum estimates.
6. We have to rely on assumptions of the composition of crust and mantle. This initial composition, however, determines the hydration/dehydration reactions that are calculated based on the thermodynamic model. A study of *Hacker* [2008] that uses a broad variety of bulk compositions for subducted materials for a global range of possible PT conditions at subduction zones demonstrates the possible effects of varying input materials to the water budget. As we do not have more specific information for our study area, we solely use a single mean "standard composition" for upper/lower crust and serpentinized mantle that has been used from many other studies dealing with similar aspects of subduction zone modeling (Table 2) [*Staudigel et al*., 1996; *Kerrick and Connolly*, 1998]. Last but not least, the model also depends on the reliability of the thermodynamic database and the water-releasing mineral reactions.
7. Our strategy assumes a hydration of crust and mantle that is uniformly dependent on age and thermal structure, as opposed to models of localized hydration along faults [*Wada et al*., 2012] because it is an easier assumption in the absence of good data on lateral variations in fault intensity. This is a point to be considered in the future.
8. Finally, we want to stress that the flux values of water released under the fore arc and arc versus transported beyond the arc strongly depend on the reference depth/position/pressure that one chooses for dividing between fore arc and back arc. This is particularly true for dewatering trends that show a steep gradient under the volcanic arc (e.g., the magenta-colored line in Figure 6). In that sense, we believe it is much more sound to discuss the trends of dewatering with ongoing subduction (like, e.g., in our Figures 5 and 6 or in the "Tokyo Subway Map" of *van Keken et al*. [2011, Figure 6]) than the absolute values.

Considering the above uncertainties, we are confident about the general pattern of water release from crust and mantle, but have to concede a certain variation range of about $\pm$30 km in x direction of the peaks of water release under the fore arc. We have arrived at this value by running sensitivity studies with different starting models for the ocean boundary geotherm.

6.3. Comparison With Other Subduction Zones

The influx of water subducted with the oceanic crust over the SVZ lies between 0.67 (for the youngest segment) and 0.7 g/m/s (for the oldest segment) as shown in Tables 3, 5 and Figure 7. These numbers lie well within the range of values of subduction zones around the world with minimum values of 0.037 and maximum values of 1.83 g/m/s [*Jarrard* 2003, Appendix, converted to SI units] and global estimates between 0.49 and 1.06 g/m/s [*Ito et al*., 1983, converted into water flux rates]. They fit particularly well with values calculated for Alaska, Kamchatka, the Aleutians, Mexico, Central America, Colombia, Peru, North and Central Chile that all are between 0.55 and 0.8 g/m/s [*Jarrard* 2003, Appendix, converted into SI units].

The influx of water with the serpentinized oceanic mantle varies over one order of magnitude over our working area (0.073–0.8 g/m/s, Tables 4, 5 and Figure 7), depending on the Nazca Plate age. *Hacker*, in a global compilation calculated values ranging from 0.14 to 1.13 g/m/s [*Hacker*, 2008, Table 3, converted into SI units]. Subduction zones with a similar slab thermal parameter Φ range of 1000–2500 [*van Keken et al*., 2011] such as of Peru, Colombia, Mexico, British Colombia, Alaska, the Aleutians, Kamchatka, and the Kuriles show the same range of flux values (0.4–0.6 g/m/s) compared to the central parts of our working area.

The fraction of water that is subducted beyond the arc along with oceanic crust and mantle ranges between 9.6% (for the youngest segment) and 88.7% (for the oldest segment) of the total water input (not considering sediments). *Hacker* [2008] provides an estimate of 53% for the fraction of water transported with crust and mantle to postarc depth in subduction zones globally [*Hacker*, 2008, Figure 12]. However, a direct comparison is difficult, as he defines postarc transport by the 4GPa isobar as cutoff, while we simply took the position of the arc and the related depth as limit. *Hacker* [2008] also provides values for the water flux beyond the arc for individual subduction zones, and here we can see that the estimates that he gives

for slabs of comparable slab thermal parameter Φ [as defined by *van Keken et al*., 2011] are ranging between 0.7 and 0.95 g/m/s [*Hacker*, 2008, Table 3, combined values, converted into SI units], which is somewhat lower than our estimate for the oldest two segments of the Nazca Plate in our working area (1.26–1.33 g/m/s, Tables 1, 5 and Figure 7), but comparable to the intermediate segment 3 (0.64 g/m/s). As the author uses the same igneous ocean crust alteration model of *Jarrard* [2003], the same thermodynamic data base and similar initial crust composition, it is most probable that our higher values for flux beyond the arc are due to the higher influx along with the serpentinized mantle that we propose. As we have modeled the degree of mantle serpentinization for the slab segments individually with the model of *Iyer et al*. [2012] we prefer our results in this case.

7. Conclusions

We observe a high variability in the water influx and outflux between the different segments of the subduction zone of southern Central Chile. The differences are entirely due to the different thermal state of the slab segments. The older and colder segments at the northern end of the subduction zone carry roughly twice as much water in the crust and mantle as the youngest segments at the southern end of the subduction zone. The release of water to the fore arc and arc, however is largest in the younger and warmer segments, as the oldest segments carry the bulk of water to postarc depth. The values of influx and outflux are in the range of values of subduction zones with similar slab thermal parameters. The high variability over a relatively short distance of $<$1500 km of subduction zone implies that it is problematic to consider subduction zones as entities when calculating global budgets.

Acknowledgments
This publication is contribution 272 of the Sonderforschungsbereich 574 "Volatiles and Fluids in Subduction Zones" at Kiel University. We thank Ingo Grevemeyer, Karthik Iyer, Jamie *Connolly*, Kelin Wang, and John He for support and discussion. The constructive comments and corrections of two anonymous reviewers are gratefully acknowledged. Supporting information is retrievable from PANGEA data repository (www.pangea.de) or by contacting the author (dvoelker@marum.de).

References

Alasonati-Tašárová, Z. (2007), Towards understanding the lithospheric structure of the southern Chilean subduction zone (36°S–42°S) and its role in the gravity field, *Geophys. J. Int.*, *170*(3), 995–1014, doi:10.1111/j.1365-246X.2007.03466.x.

Angermann, D., J. Klotz, and C. Reigber (1999), Space-geodetic estimation of the Nazca-South America Euler vector, *Earth Planet. Sci. Lett.*, *171*, 329–334, doi:10.1016/S0012-821X(99)00173-9.

Bearth, P. (1963), Chloritoid und Paragonit aus der Ophiolit-Zone von Zermatt-Saas Fee, *Schweiz. Mineral. Petrogr. Mitt.*, *43*, 269–286.

Bohm, M., S. Luth, H. Echtler, G. Asch, K. Bataille, C. Bruhn, A. Rietbrock, and P. Wigger (2002), The Southern Andes between 36 degrees and 40 degrees S latitude: Seismicity and average seismic velocities, *Tectonophysics*, *356*, 275–289.

Brown, K. M., D. M. Saffer, and B. A. Bekins (2001), Smectite diagenesis, pore-water freshening, and fluid flow at the toe of the Nankai wedge, *Earth and Planet. Sci. Lett.*, *194*, 97–109, doi:10/1016.S0012-821X(01)00546-5.

Bucher, K., and M. Frey (2002), *Petrogenesis of Metamorphic Rocks*, 341 pp., Springer, N. Y.

Cannat, M., F. Fontaine, and J. Escartín (2010), Serpentinization and associated hydrogen and methane fluxes at slow spreading ridges, in *Diversity of Hydrothermal Systems on Slow Spreading Ocean Ridges, AGU Geophys. Monogr. Ser.*, vol. 188, edited by P. A. Rona et al., pp. 241–264, AGU, Washington, D. C., doi:10.1029/2008GM000760.

Connolly, J. A. D. (2009), The geodynamic equation of state: What and how, *Geochem. Geophys. Geosyst.*, *10*, Q10014, doi:10.1029/2009GC002540.

Contreras-Reyes, E., and A. Osses (2010), Lithospheric flexure modelling seaward of the Chile trench: Implications for oceanic plate weakening in the Trench Outer Rise region, *Geophys. J. Int.*, *182*, 97–112, doi:110.1111/j.1365-1246X.2010.04629.x.

Contreras-Reyes, E., I. Grevemeyer, E. R. Flueh, M. Scherwath, and M. Heesemann (2007), Alteration of oceanic subducting lithosphere at the southern central Chile trench-outer rise, *Geochem. Geophys. Geosyst.*, *8*, Q07003, doi:10.1029/2007GC001632.

Contreras-Reyes, E., I. Grevemeyer, E. R. Flueh, and C. Reichert (2008), Upper lithospheric structure of the subduction zone offshore of southern Arauco Peninsula, Chile, at ~38°S, *J. Geophys. Res.*, *113*, B07303, doi:10.1029/2007JB005569.

Contreras-Reyes, E., E. R. Flueh, and I. Grevemeyer (2010), Tectonic control on sediment accretion and subduction off south central Chile: Implications for coseismic rupture processes of the 1960 and 2010 megathrust earthquakes, *Tectonics*, *29*, TC6018, doi:10.1029/2010TC002734.

Coombs, D. S., A. J. Ellis, W. S. Fyfe, and A. M. Taylor (1959), The zeolite facies, with comments on the interpretation of hydrothermal syntheses, *Geochim. Cosmochim. Acta*, *17*, 53–107.

Currie, C. A., R. D. Hyndman, K. Wang, and V. Kostoglodov (2002), Thermal models of the Mexico subduction zone: Implications for the megathrust seismogenic zone, *J. Geophys. Res.*, *107*(B12), 2370, doi:10.1029/2001JB000886.

Currie, C. A., K. Wang, R. D. Hyndman, and J. He (2004), The thermal effects of steady-state slab-driven mantle flow above a subducting plate: The Cascadia subduction zone and backarc, *Earth Planet. Sci. Lett.*, *223*, 35–48, doi:10.1016/j.epsl.2004.04.020.

Digel, S. G., and T. M. Gordon (1995), Phase relations in metabasites and pressure-temperature conditions at the prehnite-pumpellyite to greenschist facies transition, Flin Flon, Manitoba, Canada, in *Low-Grade Metamorphism of Mafic Rocks, Geol. Soc. Am. Spec. Pap.*, vol. 296, edited by P. Schiffman and H. W. Day, Geological Society of America, pp. 67–80.

Engdahl, E. R., R. van der Hilst, and R. Buland (1998), Global teleseismic earthquake relocation with improved travel times and procedures for depth determination, *Bull. Seismol. Soc. Am.*, *88*, 722–743.

Ernst, G. W. (1972), Occurrence and mineralogic evolution of blueschist belts with time, *Am. J. Sci.*, *272*, 657–668.

Evans, B. W. (1977), Metamorphism of alpine peridotite and serpentinite, *Ann. Rev. Earth Planet. Sci.*, *5*, 397–447.

Evans, B. W., W. Johannes, H. Oterdoom, and V. Trommsdorff (1976), Stability of chrysotile and antigorite in the serpentinite multisystem, *Schweiz. Mineral. Petrogr. Mitt.*, *56*, 79–93.

Flueh, E. R., N. Vidal, C. R. Ranero, A. Hojka, R. von Huene, J. Bialas, K. Hinz, D. Cordoba, J. J. Danobeitia, and C. Zelt (1998), Seismic investigation of the continental margin off- and onshore Valparaiso, *Tectonophysics*, *288*, 251–263, Chile.

Frey, M., C. De Capitani, and J. G. Liou (1991), A new petrogenetic grid for low-grade metabasites, *J. Metamorph. Geol.*, *9*, 497–509.
Geersen, J., J. H. Behrmann, D. Voelker, S. Krastel, C. R. Ranero, J. Diaz-Naveas, and W. R. Weinrebe (2011), Active tectonics of the South Chilean marine forearc (35°S 40°S), *Tectonics 30*, TC3006, doi:10.1029/2010TC002777.
Gieskes, J. M., P. Vrolijk, and G. Blanc (1990), Hydrogeochemistry of the Northern Barbados Accretionary Complex Transect: Ocean Drilling Project Leg 110, *J. Geophys. Res., Solid Earth*, *95*, 8809–8818, doi:10.1029/JB095iB06p08809.
Grove, T. L., N. Chatterjee, S. W. Parman, and E. Médard (2006), The influence of H_2O on mantle wedge melting, *Earth Planet. Sci. Lett.*, *249*, 74–89, doi:10.1016/j.epsl.2006.06.043.
Haberland, C., A. Rietbrock, D. Lange, K. Bataille, and S. Hofmann (2006), Interaction between forearc and oceanic plate at the South-Central Chilean margin as seen in local seismic data, *Geophys. Res. Lett.*, *33*, L23302, doi:10.1029/2006GL028189.
Hacker, B. R. (2008), H_2O subduction beyond arcs, *Geochem. Geophys. Geosyst.*, *9*, Q03001, doi:10.1029/2007GC001707.
Hacker, B. R., G. A. Abers and S. M. Peacock (2003a), Subduction factory—1: Theoretical mineralogy, densities, seismic wave speeds, and H_2O contents, *J. Geophys. Res.*, *108*(B1), 2029, doi:10.1029/2001JB001127.
Hacker, B. R., S. M. Peacock, G. A. Abers, and S. D. Holloway (2003b), Subduction factory—2: Are intermediate-depth earthquakes in subducting slabs linked to metamorphic dehydration reactions?, *J. Geophys. Res.*, *108*(B1), 2030, doi:10.1029/2001JB001129.
Hamza, V. M., and M. Munoz (1996), Heat flow map of South America, *Geothermics*, *25*, 599–646.
Harris, R. N., G. Spinelli, C. R. Ranero, I. Grevemeyer, H. Villinger, and U. Barckhausen (2010), Thermal regime of the Costa Rican convergent margin. 2: Thermal models of the shallow Middle America subduction zone offshore Costa Rica, *Geochem. Geophys. Geosyst.*, *11*, Q12S29, doi:10.1029/2010GC003273.
Herron, E. M., S. C. Cande, and B. R. Hall (1981), An active spreading center collides with a subduction zone—A geophysical survey of the Chile Margin Triple Junction, *Geol. Soc. Am. Mem.*, *154*, 683–701.
Hirajima, T., S. Banno, Y. Hiroi, and Y. Ohta (1988), Phase petrology of eclogites and related rocks from the Motalafjella high-pressure metamorphic complex in Spitsbergen (Arctic Ocean) and its significance, *Lithos*, *22*, 75–97.
Humphris, S. E., and G. Thompson (1978), Hydrothermal alteration of oceanic basalts by seawater, *Geochim. Cosmochim. Acta*, *42*, 107–125.
Ivandic, M., I. Grevemeyer, A. Berhorst, E. R. Flueh, and K. McIntosh (2008), Impact of bending related faulting on the seismic properties of the incoming oceanic plate offshore of Nicaragua, *J. Geophys. Res.*, *113*, B05410, doi:10.1029/2007JB005291.
Iyer, K., L. H. Rüpke, J. Phipps Morgan, and I. Grevemeyer (2012), Controls of faulting and reaction kinetics on serpentinization and double Benioff zones, *Geochem. Geophys. Geosyst.*, *13*, Q09010, doi:10.1029/2012GC004304.
Jacques, G., K. Hoernle, J. Gill, H. Wehrmann, I. Bindeman, and L. E. Lara (2014), Geochemical variations in the Central Southern Volcanic Zone, Chile (38–43°S): The role of fluids in generating arc magmas, *Chem. Geol.*, *371*, 27–45, doi:10.1016.j.gca.2013.05.016.
Janots, E., F. Negro, F. Brunet, B. Goffe, M. Engi, and M. L. Bouybaouene (2006), Evolution of the REE mineralogy in HP-LT metapelites of the Sebtide complex, Rif, Morocco: Monazite stability and geochronology, *Lithos*, *87*(3–4), 214–234.
Jarrard, R. D. (2003), Subduction fluxes of water, carbon dioxide, chlorine, and potassium, *Geochem. Geophys. Geosyst.*, *4*(5), 8905, doi: 10.1029/2002GC000392.
Jaupart, C., and J. C. Mareschal (1999), The thermal structure and thickness of continental roots, *Lithos*, *48*, 93–114.
Kendrick, E., M. Bevis, R. Smalley Jr., B. Brooks, R. B. Vargas, E. Lauria, and L. P. S. Fortes (2003), The Nazca-South America Euler vector and its rate of change, *J. South Am. Earth Sci.*, *16*, 125–131, doi:10.1016/S0895-9811(03)00028-2.
Kerrick, D. M., and J. A. D. Connolly (1998), Subduction of ophicarbonates and recycling of CO_2 and H_2O, *Geology*, *26*, 375–378.
Kerrick, D. M., and J. A. D. Connolly (2001), Metamorphic devolatilization of subducted oceanic metabasalts: Implications for seismicity, arc magmatism and volatile recycling, *Earth Planet. Sci. Lett.*, *189*, 19–29, doi:10.1016/S0012-821X(01)00347-8.
Kirby, S. H., W. B. Durham, and L. A. Stern (1991), Mantle phase changes and deep-earthquake faulting in subducting lithosphere, *Science*, *252*, 216–225.
Lange, D., A. Rietbrock, C. Haberland, K. Bataille, T. Dahm, F. Tillmann, and E. R. Flueh (2007), Seismicity and geometry of the South Chilean subduction zone (41.5°S–43.5°S): Implications for controlling parameters, *Geophys. Res. Lett.*, *34*, L06311, doi:10.1029/2006GL029190.
Lefeldt, M., I. Grevemeyer, J. Goßler, and J. Bialas (2009), Intraplate seismicity and related mantle hydration at the Nicaraguan trench outer rise, *Geophys. J. Int.*, *178*, 742–752, doi:10.1111/j.1365-246X.2009.04167.x.
Lefeldt, M., C. R. Ranero, and I. Grevemeyer (2012), Seismic evidence of tectonic control on the depth of water influx into incoming oceanic plates at subduction trenches, *Geochem. Geophys. Geosyst.*, *13*, Q05013, doi:10.1029/2012GC004043.
Lippard, S. J., A. W. Shelton, and I. G. Gass (1986), The ophiolite of Northern Oman, *Mem. Geol. Soc. London*, *11*, 1–178.
Liu, J., S. R. Bohlen, and W. G. Ernst (1996), Stability of hydrous phases in subducting oceanic crust, *Earth Planet. Sci. Lett.*, *143*(1–4), 161–171.
Malvoisin, B., F. Brunet, J. Carlut, S. Roumejon, and M. Cannat (2012), Serpentinization of oceanic peridotites. 2: Kinetics and processes of San Carlos olivine hydrothermal alteration, *J. Geophys. Res.*, *117*, B04102, doi:10.1029/2011JB008842.
Martin, B., and W. S. Fyfe (1970), Some experimental and theoretical observations on kinetics of hydration reactions with particular reference to serpentinization, *Chem. Geol.*, *6*, 185–202.
Matthews, A., and M. Schliestedt (1984), Evolution of the blueschist and greenschist facies rocks of Sifnos, Cyclades, Greece—A stable isotope study of subduction-related metamorphism, *Contrib. Mineral. Petrol.*, *88*(1–2), 150–163.
Müller, D., M. Sdrolias, C. Gaina, and W. R. Roest (2008), Age, spreading rates, and spreading asymmetry of the world's ocean crust, *Geochem. Geophys. Geosyst.*, *9*, Q04006, doi:10.1029/2007GC001743.
Natland, J. H., and H. J. B. Dick (2001), Formation of the lower ocean crust and the crystallization of gabbroic cumulates at a very slowly spreading ridge, *J. Volcanol. Geotherm. Res.*, *110*(3–4), 191–233.
Okamoto, A., Y. Ogasawara, Y. Ogawa, and N. Tsuchiya (2011), Progress of hydration reactions in olivine-H_2O and orthopyroxenite-H_2O systems at 250 degrees C and vapor-saturated pressure, *Chem. Geol.*, *289*, 245–255, doi:10.1016/j.chemgeo.2011.08.007.
Ono, S. (1998), Stability limits of hydrous minerals in sediment and mid-ocean ridge basalt compositions: Implications for water transport in subduction zones, *J. Geophys. Res.*, *103*(B8), 18,253–18,267.
Padron-Navarta, J. A., J. Hermann, C. J. Garrido, V. L. Sanchez-Vizcaino, and M. T. Gomez-Pugnaire (2010), An experimental investigation of antigorite dehydration in natural silica-enriched serpentinite, *Contrib. Mineral. Petrol.*, *159*(1), 25–42.
Patrick, B. E., and H. W. Day (1989), Controls on the first appearance of jadeitic pyroxene, northern Diablo Range, California, *J. Metamorph. Geol.*, *7*, 629–639.
Pawley, A. R., S. A. T. Redfern, and B. J. Wood (1995), Thermal expansivities and compressibilities of hydrous phases in the system MgO-SiO_2-H_2O: Talc, phase A and 10-angstrom phase, *Contrib. Mineral. Petrol.*, *122*, 301–307.
Peacock, S. M. (1993), The importance of blueschist—Eclogite dehydration reactions in subducting oceanic crust, *Geol. Soc. Am. Bull.*, *105*(5), 684–694.

Peacock, S. M., and K. Wang (1999), Seismic consequences of warm versus cool subduction metamorphism: Examples from southwest and northeast Japan, *Science*, *286*, 937–939.
Peacock, S. M., P. E. van Keken, S. D. Holloway, B. R. Hacker, G. A. Abers and R. L. Fergason (2005), Thermal structure of the Costa Rica—Nicaragua subduction zone, *Phys. Earth Planet. Inter.*, *149*(1–2), 187–200, doi:10.1016/j.pepi.2004.08.030.
Poli, S., and M. W. Schmidt (1995), H_2O transport and release in subduction zones—Experimental constraints on basaltic and andesitic systems, *J. Geophys. Res.*, *100*(B11), 22,299–22,314.
Powell, W. G., D. M. Carmichael, and C. J. Hodgson (1993), Thermobarometry in a subgreenschist to greenschist transition in metabasites of the Abitibi greenstone-belt, Superior-Province, Canada, *J. Metamorph. Geol.*, *11*, 165–178.
Ranero, C. R., J. P. Morgan, K. McIntosh, and C. Reichert (2003), Bending-related faulting and mantle serpentinization at the Middle America Trench, *Nature*, *425*, 376–373, doi:10.1038/nature0196.
Rotman, H. M. M., and G. A. Spinelli (2014), Remarkably consistent thermal state of the south central Chile subduction zone from 36°S to 45°S, *J. Geophys. Res. Solid Earth*, *119*, 3503–3516, doi:10.1002/2013JB010811.
Rudnick, R. L., W. F. McDonough, and R. J. O'Connell (1998), Thermal structure, thickness and composition of continental lithosphere, *Chem. Geol.*, *145*, 395–411.
Rüpke, L. H., J. P. Morgan, M. Hort, and J. A. D. Connolly (2004), Serpentine and the subduction zone water cycle, *Earth Planet. Sci. Lett.*, *223*, 17–23, doi:10.1016/j.epsl.2004.04.018.
Saffer, D. M. (2003), Pore pressure development and progressive dewatering in underthrust sediments at the Costa Rican subduction margin: Comparison with northern Barbados and Nankai, *J. Geophys. Res.*, *108*(B5), 2261, doi:10.1029/2002JB001787.
Scherwath, M., E. Contreras-Reyes, E. R. Flueh, I. Grevemeyer, A. Krabbenhoeft, C. Papenberg, C. J. Petersen, and R. W. Weinrebe (2009), Deep lithospheric structures along the southern central Chile Margin from wide-angle P-wave modelling, *Geophys. J. Int.*, *179*, 579–600, doi:10.1111/j.1365-246X.2009.04298.x.
Schmidt, M. W., and S. Poli (1998), Experimentally based water budgets for dehydrating slabs and consequences for arc magma generation, *Earth Planet. Sci. Lett.*, *163*, 361–379.
Siebert, L., and T. Simkin (2002), *Volcanoes of the World: An Illustrated Catalog of Holocene Volcanoes and Their Eruptions, Global Volcanism Prog. Digital Inform. Ser.*, Smithsonian Inst., Washington, D. C. [Available at http://www.volcano.si.edu/world/.]
Sisson, T. W., and T. L. Grove (1993), Temperature and H_2O contents of low-MgO high-alumina basalts, *Contrib. Mineral. Petrol.*, *113*, 143–166.
Skelton, A., R. Whitmarsh, F. Arghe, P., Crill, and H. Koyi (2005), Constraining the rate and extent of mantle serpentinization from seismic and petrological data: Implications for chemosynthesis and tectonic processes, *Geofluids*, *5*, 153–164, doi:10.1111/j.1468-8123.2005.00111.x.
Springer, R. K., H. W. Day, and R. E. Beiersdorfer (1992), Prehnite-pumpellyite to greenschist facies transition, Smartville complex, near Auburn, California, *J. Metamorph. Geol.*, *10*, 147–170.
Staudigel, H., T. Plank, B. White, and H.-U. Schmincke (1996), Geochemical fluxes during seafloor alteration of the basaltic upper oceanic Crust: DSDP sites 417 and 418, in *Subduction Top to Bottom, Geophys. Monogr. Ser.*, pp. 19–38, AGU, Washington, D. C., doi:10.1029/GM096p0019.
Stein, C., and S. Stein (1992), A model for the global variation in oceanic depth and heat flow with lithospheric age, *Nature*, *359*, 123–128.
Stern, C. R., H. Moreno, L. Lopez-Escobar, J. E. Clavero, L. E. Lara, J. A. Naranjo, M. A. Parada, M. A. Skewes (2007), Chilean volcanoes, in edited by T. Moreno and W. Gibbons, The geology of Chile., pp. 147–178, Geological Society of London, London, U. K.
Stern, C. R. (2004), Active Andean volcanism: Its geologic and tectonic setting, *Rev. Geol. Chile*, *31*, 161–206.
Stern, C. R. (2011), Subduction erosion: Rates, mechanisms, and its role in arc magmatism and the evolution of the continental crust and mantle, *Gondwana Res.*, *20*, 284–308, doi:10.1016/j.gr.2011.1003.1006.
Syracuse, E. M., and G. A. Abers (2006), Global compilation of variations in slab depth beneath arc volcanoes and implications, *Geochem. Geophys. Geosyst.*, *7*, Q05017, doi:10.1029/2005GC001045.
Syracuse, E. M., P. E. van Keken, and G. A. Abers (2010), The global range of subduction zone thermal models, *Phys. Earth Planet. Inter.*, *183*, 73–90.
Tassara, A., H. J. Götze, S. Schmidt, and R. Hackney (2006), Three-dimensional density model of the Nazca plate and the Andean continental margin, *J. Geophys. Res.*, *111*, B09404, doi:10.1029/2005JB003976.
Tebbens, S. F., S. C. Cande, L. Kovacs, J. C. Parra, J. L. LaBrecque, and H. Vergara (1997), The Chile Ridge: A tectonic framework, *J. Geophys. Res.*, *102*(B6), 12,035–12,059.
Thompson, A. B. (1971), Analcite-albite equilibria at low temperatures, *Am. J. Sci.*, *271*, 79–92.
Tomasson, J., and H. Kristmansdottir (1972), High-temperature alteration minerals and thermal brines, Reykjanes, Iceland, *Contrib. Mineral. Petrol.*, *36*, 123–134.
Triboulet, C. (1992), The (Na-Ca)-amphibole albite chlorite epidote quartz geothermobarometer in the system S-A-F-M-C-N-H_2O. 1: An empirical calibration, *J. Metamorph. Geol.*, *10*(4), 545–556.
Trommsdorff, V., and B. W. Evans (1972), Progressive metamorphism of antigorite schist in Bergell tonalite aureole (Italy), *Am. J. Sci.*, *272*, 423–437.
Tsujimori, T., and W. G. Ernst (2014), Lawsonite blueschists and lawsonite eclogites as proxies for palaeo-subduction zone processes: A review, *J. Metamorph. Geol.*, *32*(5), 437–454.
Ukar, E., and M. Cloos (2014), Low-temperature blueschist-facies mafic blocks in the Franciscan melange, San Simeon, California: Field relations, petrology, and counterclockwise P-T paths, *Geol. Soc. Am. Bull.*, *126*(5–6), 831–856.
Ulmer, P., and V. Trommsdorff (1995), Serpentine stability to mantle depths and subduction-related magmatism, *Science*, *268*, 858–861.
van Keken, P. E., et al. (2008), A community benchmark for subduction zone modeling, *Phys. Earth Planet. Inter.*, *171*, 187–197, doi:10.1016/j.pepi.2008.04.015.
van Keken, P. E., B. R. Hacker, E. M. Syracuse, and G. A. Abers (2011), Subduction factory. 4: Depth-dependent flux of H2O from subducting slabs worldwide, *J. Geophys. Res.*, *116*, B01401, doi:10.1029/2010JB007922.
Völker, D., I. Grevemeyer, M. Stipp, K. Wang, and J. He (2011a), Thermal control of the seismogenic zone of southern central Chile, *J. Geophys. Res.*, *116*, B10305, doi:10.1029/2011JB008247.
Völker, D., S. Kutterolf, and H. Wehrmann (2011b), Comparative mass balance of volcanic edifices at the southern volcanic zone of the Andes between 33°S and 46°S, *J. Volcanol. Geotherm. Res.*, *205*, 114–129, doi:110.1016/j.jvolgeores.2011.1003.1011.
Völker, D., J. Geersen, E. Contreras-Reyes, and C. Reichert (2013), Sedimentary fill of the Chile Trench (32°S–46°S): Volumetric distribution and causal factors, *J. Geol. Soc.*, *170*(5), 723–736, doi:10.1144/jgs2012-119.

Wada, I., and K. Wang (2009), Common depth of slab-mantle decoupling: Reconciling diversity and uniformity of subduction zones, *Geochem. Geophys. Geosyst.*, *10*, Q10009, doi:10.1029/2009GC002570.

Wada, I., K. Wang, J. He, and R. D. Hyndman (2008), Weakening of the subduction interface and its effects on surface heat flow, slab dehydration, and mantle wedge serpentinization, *J. Geophys. Res.*, *113*, B04402, doi:10.1029/2007JB005190.

Wada, I., M. D. Behn, and A. M. Shaw (2012), Effects of heterogeneous hydration in the incoming plate, slab rehydration and mantle wedge hydration on slab-derived H_2O flux in subduction zones, *Earth Planet. Sci. Lett.*, *353–354*, 60–71.

Wang, K., and J. H. He (2008), Effects of frictional behavior and geometry of subduction fault on coseismic seafloor deformation, *Bull. Seismol. Soc. Am.*, *98*, 571–579, doi:10.1785/0120070097.

Wang, K., and Y. Hu (2006), Accretionary prisms in subduction earthquake cycles: The theory of dynamic Coulomb wedge, *J. Geophys. Res.*, *111*, B06410, doi:10.1029/2007GC001721.

Wegner, W. W., and W. G. Ernst (1983), Experimentally determined hydration and dehydration reaction rates in the system $MgO\text{-}SiO_2\text{-}H_2O$, *Am. J. Sci.*, *283-A*, 151–180.

Weinrebe, W. R., and M. Hasert (2012), Bathymetric Charts of the South East Pacific with links to gridded datasets, doi:10.1594/PANGAEA.785515, Digital data set, hosted by PANGEA data repository. [Available at www.pangea.de.]

Will, T. M., R. Powell, T. Holland, and M. Guiraud (1990), Calculated greenschist facies mineral equilibria in the $CaO\text{-}FeO\text{-}MgO\text{-}Al_2O_3\text{-}SiO_2\text{-}CO_2\text{-}H_2O$-system, *Contrib. Mineral. Petrol.*, *104*, 353–368.

Wunder, B., and W. Schreyer (1997), Antigorite: High pressure stability in the system $MgO\text{-}SiO_2\text{-}H_2O$ (MSH), *Lithos*, *41*, 213–227.